Published in final edited form as:
Nature. 2020 August ; 584(7821): 470–474. doi:10.1038/s41586-020-2505-4.

A universal tradeoff between growth and lag in fluctuating environments

Markus Basan[1,2,¶,*], **Tomoya Honda**[3,4,*], **Dimitris Christodoulou**[2], **Manuel Hörl**[2], **Yu-Fang Chang**[1], **Emanuele Leoncini**[1], **Avik Mukherjee**[1], **Hiroyuki Okano**[3], **Brian R. Taylor**[3], **Josh M. Silverman**[5], **Carlos Sanchez**[1], **James R. Williamson**[5], **Johan Paulsson**[1], **Terence Hwa**[3,4,¶], **Uwe Sauer**[2,¶]

[1]Department of Systems Biology, Harvard Medical School, Boston, MA 02115, USA. [2]Institute of Molecular Systems Biology, ETH Zürich, 8093 Zürich, Switzerland. [3]Department of Physics, University of California at San Diego, La Jolla, CA 92093 USA. [4]Section of Molecular Biology, Division of Biological Sciences, University of California at San Diego, La Jolla, CA 92093 USA. [5]Department of Integrative Structural and Computational Biology, and The Skaggs Institute for Chemical Biology, The Scripps Research Institute, La Jolla, CA 92037, USA.

Abstract

The rate of cell growth is crucial for bacterial fitness and a main driver of proteome allocation[1,2], but it is unclear what ultimately determines growth rates in different environmental conditions. Increasing evidence suggests that other objectives also play key roles[3–7], such as the rate of physiological adaptation to changing environments[8,9]. The challenge for cells is that these objectives often cannot be independently optimized, and maximizing one often reduces another. Many such tradeoffs have indeed been hypothesized, based on qualitative correlative studies[8–11]. Here we report the occurrence of a tradeoff between steady-state growth rate and physiological adaptability for *Escherichia coli*, upon abruptly shifting a growing culture from a preferred carbon source to fermentation products such as acetate. Such transitions, common for enteric bacteria, are

---

[¶]Correpondences should be addressed to Markus Basan (markus@hms.harvard.edu), Terence Hwa (thwa@ucsd.edu) or Uwe Sauer (sauer@imsb.biol.ethz.ch).

[*]These authors contributed equally: Markus Basan, Tomoya Honda

Contributions
M.B., T. Hwa and U.S. designed the study. Experiments were performed by M.B., T. Honda, M.H., Y.C., E.L., A.M., H.O., B.T., J.M.S., and C.S. and all authors contributed to the analysis of experimental data. Specifically, lag times for *E. coli* were measured by M.B. and T. Honda. Metabolite measurements and analysis were performed by M.B. and M.H. Proteomics measurements were performed by T. Honda, and H.O. Proteomics data analysis was performed by T. Honda, D.C. and J.M.S. Genetic constructs were made by M.B. and Y.C. Lag times for *Saccharomyces cerevisiae* and *Bacillus subtilis* were measured by Y.C. Growth rates for *Bacteroides thetaiotaomicron* were measured by B.T. Experiments for single cell lag phases from microfluidics and plates were performed and analyzed by E.L., A.M. and C.S. M.B., D.C., T. Hwa and U.S. developed the model. M.B., J.P., T. Hwa and U.S. wrote the paper and the Supplementary Information.

Ethics declarations
The authors declare no competing financial or non-financial interest.

Data availability
Source data for all figures is publicly available. Lag times are provided in Table S2–S3 in the Supplementary Information. All other data is found in downloadable Excel files for each figure. Data from Fig. 3a was taken from Hui *et al.*[3] and is deposited on the journal website.

often accompanied by multi-hour lags before growth resumes. Metabolomic analysis revealed that the long lags resulted from the depletion of key metabolites due to the sudden reversal of central carbon flux imposed by these nutrient shifts. A model of sequential flux limitation not only explained the observed universal tradeoff between growth and adaptability, but also generated quantitative predictions that were validated experimentally. The observed trade-off reflects the opposing enzyme requirements for glycolysis versus gluconeogenesis.

To study the interrelation between the rate of cell growth and the rate of physiological adaptation (characterized by the inverse of the “lag time” defined in Fig. 1a), we shifted wild-type *Escherichia coli* (Table S1) between two minimal media, each containing a single carbon source. Defined postshift conditions and very rapid environmental changes were implemented as “complete shifts” that ensure no preshift carbon source was available to cells in the postshift medium (Fig. 1b). We first investigated shifts from different glycolytic carbon sources into acetate, a gluconeogenic carbon source that requires fluxes through glycolysis to reverse direction. Because acetate is the primary fermentation product of many bacteria, including *E. coli*, it is naturally available to these bacteria upon the exhaustion of the primary carbon source.

When quantified by lag time, defined as the integrated time lost during the adaptation to new conditions compared to an immediate response (Fig. 1a), these shifts exhibited extended lags of up to 10 hours (Fig. 1c circles), much longer than the doubling times in preshift and postshift media (< 2 hours), and often included periods without detectable biomass production lasting several hours (Extended Data Fig. 1a). A striking correlation emerged between the growth rate in the preshift medium and the lag time, (circles, Fig. 1c), i.e., fast growing cells took a long time to adjust to the new medium while slow growing cells resumed growth much more quickly. The same relation was obtained when preshift growth was varied by titrating the uptake rates of lactose as an example of a glycolytic carbon source (squares, Fig. 1c), suggesting that the relation between preshift growth and lag times is dependent on the carbon influx rate rather than the specifics of the preshift carbon sources. A similar pattern was found for population growth dynamics with chemostat-controlled growth rates[12]. The data in Fig. 1c shows that lag times (T_{lag}) increased with increasing preshift growth rate (λ_{pre}), with an apparent divergence at a critical growth rate λ_0. Indeed, re-plotting the data of Fig. 1c reveals an approximately linear relation (purple symbols and line in Fig. 1d) between the inverse lag time $1/T_{lag}$, a measure of adaptability, and λ_{pre}, i.e.,

$$1/T_{lag} = \alpha \cdot (\lambda_0 - \lambda_{pre}), \qquad [1]$$

where α is a dimensionless proportionality constant.

To test the generality of this relation, we analyzed lag times in 144 transitions (see Tables S2 & S3), yielding long lag times for shifts from six glycolytic to six gluconeogenic carbon sources (Extended Data Fig. 2a–f). Strikingly, all these shifts exhibited similar linear relations between the preshift growth rate and inverse lag time, but with different proportionality constants α for different postshift carbon sources, all with the same critical growth rate λ_0 ≈1.1/hr (see Fig. 1d & Extended Data Fig. 2). Some degree of correlation exists also between the lag time and postshift growth rates (Extended Data Fig. 2g) as observed previously[13], but the pattern is much weaker compared to those in Fig. 1c, 1d. We also examined several classic diauxic shifts, where both carbon sources are present in preshift, and the lag times were found to be almost identical to those from the complete shifts that we study here in most cases (Extended Data Fig. 1b–d).

To investigate the origin of the extended lag time in our shifts, we first tested if dormant and heterogeneous subpopulations may play a role. Using two complementary methods (see Supplementary Note 1, Extended Data Figure 3, 4), we quantified cell-to-cell variability following the shift from glucose to acetate. The results revealed some heterogeneity in lag times, but no distinct subpopulations: None of the cells resumed growth immediately after the shift, and virtually all cells resumed growth shortly after the average lag time.

To determine if the observed correlation between lag time and preshift growth is due to a limitation in central metabolism (referred to as “metabolic limitation”), we quantified metabolite pools throughout the lag phase of the glucose-to-acetate transition (Fig. 2a). By comparing the dynamics of metabolite pools and fluxes with steady-state levels during exponential growth on glucose and acetate, we can infer metabolic bottlenecks. Remarkably, over the course of the lag phase, the concentrations of different metabolites increased in a sequential manner (Fig. 2b) that matched their position in gluconeogenesis: Metabolites in the tricarboxylic acid (TCA) cycle (citrate, malate) started to accumulate 1–2 hours into the lag phase and also overshot their postshift steady-state values (dashed black line, Fig. 2b) by several-fold once growth resumed ~4 hr after shift (Fig. 2a). The levels of metabolites in upper glycolysis increased even later (Fig. 2b & Extended Data Fig. 5a). Importantly the increase of the latter coincided with the time of growth resumption (Fig. 2a). In particular, the pool of the key regulatory metabolite fructose-1–6-bisP (FBP) plunged rapidly by 200-fold within 30 minutes of the shift and remained well below its postshift steady-state level until 30 minutes before growth resumption (see Extended Data Fig. 5c). This finding is not compatible with the mechanism recently proposed to underlie lag phases to gluconeogenesis based on a postulated high FBP pool in the majority of the cell population during lag phase[12].

Estimating the fluxes by multiplying measured metabolite concentrations and the turnover rates derived from ^{13}C-labeling dynamics, we observed a sequential pattern that followed their position in gluconeogenesis (Fig. 2c). TCA cycle metabolites quickly became fully ^{13}C-labeled. In contrast, gluconeogenic flux to upper glycolysis was hardly detectable even 30 minutes after the shift, and was still below 1% of the steady-state level 1.5 hours after shift.

The observed metabolic dynamics suggest that gluconeogenic flux limits biosynthesis of biomass components derived from intermediates in upper glycolysis. In particular, metabolites like erythrose-4-P and ribose-5-P, branching off from upper glycolysis and required for the biosynthesis of specific amino acids and nucleotides, may limit biomass production. Because biomass synthesis requires fixed stoichiometric ratios of building blocks, metabolites in TCA cycle and lower glycolysis accumulate far beyond their steady state concentrations (Fig. 2b), since they cannot be incorporated into biomass without sufficient metabolites in upper glycolysis. In accordance with this hypothesis, we found the absolute concentrations of key metabolites in upper glycolysis (e.g. F6P) to be small compared to the affinity constants of the key enzymes required for the production of erythrose-4-P and ribose-5-P (Table S4) .

After the shift to acetate, gluconeogenic flux is essential for biomass production and enzyme synthesis. While many glycolytic enzymes are reversible and can thereby also catalyze gluconeogenesis, several glycolytic reactions are thermodynamically strongly favored in the glycolytic direction such that they can be considered effectively irreversible. As illustrated in Fig. 2d, in a simplified picture of central metabolism, gluconeogenesis can be considered as a linear pathway consisting of “lower gluconeogenenic” reactions (catalyzed by phosphoenolpyruvate carboxykinase: Pck; malate dehydrogenases: MaeA, MaeB; phosphoenolpyruvate synthetase: Pps) and “upper gluconeogenic” reactions (catalyzed primarily by the essential enzyme fructose-1,6-bisphosphatase: Fbp). These dedicated gluconeogenic enzymes are required for gluconeogenesis but many of them are lowly expressed during preshift growth and immediately after the shift, when compared to their abundances in postshift steady state (Extended Data Fig. 6), presumably because the activities of the gluconeogenic enzymes can lead to substantial futile cycling that dissipates energy. Consistent with the observed lag time increase with higher preshift growth rates (Fig. 1c), the abundances of the lower gluconeogenic enzymes (quantified by proteomics in a previous work[3]) decease with higher preshift growth rates (Fig. 3a).

Quantitative proteomics measurements showed that the abundances of gluconeogenic enzymes increased very gradually, coinciding with exit from the lag phase (Extended Data Fig. 6). During the lag phase, formation of these lower gluconeogenic enzymes requires precursors (e.g. specific amino acids), whose synthesis rate is in turn limited by the gluconeogenic flux. Hence, right after the shift, the cell is trapped in a state where a bottleneck in gluconeogenic flux limits the synthesis of amino acids, and hence the production of enzyme needed to alleviate this bottleneck (Extended Data Fig. 7a). Indeed, reducing the requirements of metabolites resulting from gluconeogenic flux such as erythrose-6-phosphate by addition of the three aromatic amino acids derived from it (Trp, Phe, Tyr) to the postshift medium (Fig. 2e), reduced the lag time by ~50%, even though individually these amino acids do not support growth[14].

For rapid adaptations dominated by simple catabolic bottlenecks, a kinetic model of growth adaptation based on the dynamic reallocation of proteomic resources was shown recently to give quantitatively accurate descriptions of adaptation dynamics[15]. However for the very long lag phases studied here, severe internal metabolic bottlenecks are involved due to the reversal of central carbon fluxes. Guided by the metabolomic and proteomic data (Figs. 2), we constructed a minimalistic mathematical model. The gluconeogenic flux is assumed to be the bottleneck for amino acid synthesis required for *de novo* production of gluconeogenic enzymes during the lag phase (illustrated in Extended Data Fig. 7a and resulting in Eq. [a] in that figure). As illustrated in Extended Data Fig. 7b and explained in Supplementary Note 2, the gluconeogenic flux is determined by the scaling of metabolite concentrations at the lower and upper gluconeogenesis, which are in turn determined by the levels of lower gluconeogenic enzymes (resulting in Eq. [b] in that figure). Solving the resulting differential equation, we arrived at a simple expression for the inverse lag time:

$$1/T_{lag} \propto \quad \phi^{pre}_{GNG,\ lower}, \qquad [2]$$

where $\phi^{pre}_{GNG,\ lower}$ denotes the preshift abundance of lower gluconeogenic enzymes that provide the initial condition. The abundances of these enzymes rise throughout the lag phase (Extended Data Fig. 6) and their abundances in preshift conditions[14] are well described by a linear decrease with increasing preshift growth rate, λ_{pre}, i.e.,

$$\phi^{pre}_{GNG,\ lower} \propto \left(\lambda_C - \lambda_{pre}\right), \qquad [3]$$

vanishing at a characteristic growth rate, $\lambda_C \approx 1.1$/hr (lines in Fig. 3a). This resembles the linear cAMP-mediated increase of catabolic protein abundances for carbon-limited growth[14]. Inserting this growth-rate dependence into Eq. [2], we obtain $1/T_{lag} \propto (\lambda_C - \lambda_{pre})$, which is identical to the empirical relation Eq. [1], with the same critical growth rate $\lambda_0 \approx$ 1.1/hr. Thus, our model successfully recapitulates the observed growth rate-lag time relations (Fig. 1d) up to an overall scaling factor α (Eq. [1]).

Lag times for most postshift carbon sources collapse on the same curve (black curve, Fig. 1d & Extended Data Fig. 2). However, shifts to acetate are described by a different scaling factor α (magenta symbols and line), and a milder deviation for shifts to malate (green circles and line). A possible explanation for the altered acetate line is that only growth on acetate requires the glyoxylate shunt in addition to other gluconeogenic enzymes. If true, then pre-expressing enzymes of the glyoxylate shunt (AceB and AceA) should eliminate this additional bottleneck and revert the relation between lag time and growth rate to that observed for shifts to most other TCA cycle substrates (black line, Fig. 1d & Extended Data Fig. 2). Indeed, preshift expression of the glyoxylate bypass reduced the lag times for various shifts to acetate (compare red circles and magenta curve in Fig. 3b), such that the reduced lag times actually fall on the relation followed by most other gluconeogenic substrates as predicted (black curve, Fig. 3b).

To directly test the prediction of a linear relation between the inverse lag time and the abundance of lower gluconeogenic enzymes (Eq. [2]), we considered a shift from glucose to pyruvate, where a single gluconeogenic enzyme, phosphoenolpyruvate synthetase (PpsA), is required for the lower gluconeogenic reaction. We constructed a strain with linearly titratable PpsA expression that had a negligible effect on preshift growth. Titrating PpsA expression indeed affected the lag time of the glucose-to-pyruvate shift and the model prediction was quantitatively validated by the observed proportionality between the preshift induction level of PpsA and inverse lag time (Fig. 3c) over a 5-fold range in lag times. Since the full induction of PpsA in postshift alone was insufficient to overcome the lag phase, whereas preshift induction resulted in a large reduction of lag time, our results demonstrate the importance of expressing gluconeogenic enzymes in glycolytic conditions to shorten lag phase.

An important remaining question is why *E. coli* cannot avoid the depletion of gluconeogenic metabolite pools after shift to gluconeogenesis. We hypothesized that allosteric regulation of the opposing glycolytic enzymes by metabolic intermediates does not achieve a complete inhibition of their activities during lag phase. To test whether residual activity of glycolytic enzymes may be a significant cause of long lag, we overexpressed glycolytic enzymes catalyzing irreversible reactions in preshift conditions. Indeed, this severely impaired the switch from glycolysis to gluconeogenesis, more than doubling the lag time in most cases, as compared to preshift overexpression of a control enzyme (Extended Data Fig. 8). As glycolytic enzymes are abundant throughout the lag phase of wild-type strain (Extended Data Fig. 6), the transition from glycolysis to gluconeogenesis is likely dominated by futile cycling, with both gluconeogenic and glycolytic enzymes active and working in opposite directions.

In this study, we have established a series of low metabolite pools in gluconeogenesis as the cause of long lags during the transition from glycolysis. This is because for fast glycolytic growth, the distribution of enzymes strongly favor glycolysis over the opposing gluconeogenesis (Extended Data Fig. 7c). At lower glycolytic fluxes such as on poor glycolytic substrates, the change in the enzyme distribution (lower glycolytic enzyme and higher gluconeogenic enzyme abundances) favors glycolysis less, and the transition to gluconeogenic growth becomes faster. Thus, the two important fitness measures, growth rate and adaptability (inverse lag time), are constrained as captured by Eq. [1]. As this simple empirical relation holds broadly for many pairs of carbon sources tested (Fig. 1d & Extended Data Fig. 2), we propose Eq. [1] be considered a phenomenological law of the growth-adaptation tradeoff, with the quantitative form arising from the structure of central carbon metabolism as suggested by the model described in Extended Data Fig. 7.

The existence of this tradeoff suggests that it might be advantageous for cells to choose slower growth for the benefit of shorter lag, in anticipation of switching to gluconeogenesis when the primary glycolytic substrates run out. It provides a unique perspective towards understanding the notorious problem of why bacteria grow on different substrates at broadly disparate rates. Hence, the quality of a substrate as measured by growth rate is a reflection of the ecological likelyhood that conditions will change in fluctuating natural environments or across the bacterial infectious cycle, rather than based on fundamental biochemical properties of the substrate, e.g. its energy content. As an example, wildtype *E. coli* grew substantially more slowly on fructose and mannose compared to glucose despite their similar chemical properties. A knockout of the transcriptional regulator Cra, which activates the expression of gluconeogenic enzymes while repressing those of glycolytic enzymes, increased growth on both fructose and mannose (Extended Data Fig. 9a), but is unable to shift to many gluconeogenic substrates. Thus, Cra may be designated to hold back the growth of wildtype cells on glycolytic substrates to enable a swift shift to gluconeogenesis when necessary. More striking is the growth on glycerol, often thought of as a poor nutrient compared to glucose due to reduced energy content. Yet, a single-residue mutation in the glycerol uptake protein GlpK, which increases its uptake efficiency, increases growth on glycerol by over 20%[16,17]. This faster growing mutant has been extensively characterized[18], but a disadvantage of this mutation was only demonstrated previously when combined with additional mutations[19], raising the possibility that *E. coli* may be simply maladapted to glycerol. Guided by our model, we find this mutant to exhibit a substantially longer lag compared to the slower-growing wildtype (Fig. 3d), suggesting that slower growth of wildtype *E. coli* on glycerol might be selected to reduce the lag time upon abrupt transition to gluconeogenic substrates in the natural habitat.

This growth-adaptation tradeoff can be turned into a quantitative criterion for selecting the rate of cell growth (λ), by minimizing the total time for growth on a glycolytic substrate (~1/λ) together with its subsequent lag, $T_{lag}(\lambda)$ (Eq. [1]). Using parameters for the *E.coli* strain characterized in this study and assuming the environment provides glycolytic substrate at a concentration that would support bacterial growth by a factor N (Extended Data Fig. 10a), we obtain an optimal glycolytic growth rate λ^* for which the time spent on growth and lag is balanced and minimized (Extended Data Fig. 10b).

Interestingly, values for the optimal growth rate range from 0.5/hr to 1/hr for a broad range nutrient abundances (Extended Data Fig. 10c), coinciding rather well with the range of growth rates observed for our strain on different glycolytic carbon sources[2]. The growth-adaptation tradeoff may thus be an important factor in the evolutionary selection of growth rate on specific substrates.

Although our study was focused on *E. coli*, we expect a similar tradeoff in other microbes because the biochemical structure of central metabolism is highly conserved. For anaerobic bacteria, which typically do not grow on gluconeogenic carbon sources, our model would predict a lack of tradeoff such that fast growth would be selected for many carbon sources. Indeed, the gut anaerobe *Bacteroides thetaiotaomicron* grows at similarly fast rater on several tested carbon sources; see Extended Data Fig. 9e. We also confirmed the existence of the tradeoff in the strictly aerobic bacterium *Bacillus subtilis* and in two wild-type strains of the lower eukaryote *Saccharomyces cerevisiae* (see Extended Data Fig. 9b–d).

Recent studies have identified multiple, conflicting objectives affecting microbial phenotypes[8–10,20–22], e.g., between growth and motility[2,23,24], or between growth and survival[25–27]. The establishment of quantitative relations for these and other pairs of conflicting traits can be expected to connect apparently disparate fitness measures into a unified framework. Identifying their occurrences and elucidating their origins will be crucial for gaining a better understanding of the diversity of microbial phenotypes across conditions and across species.

Methods

a, glucose to acetate; **b,** glucose to pyruvate; **c,** glucose to malate; **d,** glucose to succinate.

Strain construction

All *E. coli* strains used in this study are derived from K-12 NCM3722[30]. *B. thetaiotaomicron* was obtained from the American Type Culture Collection (ATCC 29148).

Construction of P*tet-aceB* and P*tet-ppsA* strains (NQ1350, NQ1357): The DNA region containing the km^r gene, *rrnB*T and the promoter Ptet of the pKDT P*tet* plasmid[31] was PCR amplified with upstream and downstream primers ptet-aceB-insert-F / ptet-aceB-insert-R and Ptet-ppsA-insert-F / Ptet-ppsA-insert-R respectively and subsequently integrated into the chromosome of *E. coli* strain NQ309 to replace the chromosomal promoters of *aceB* and *ppsA* (each from -150 bp untill -1 bp relative to transcriptional start site)[32]. Each of the P*tet*-promoter substitutions was then transferred to NQ1358 (NCM3722 ycaD: P*tet-tetR Δ* Km^r)[31] backgrounds by phage P1 *vir* mediated transduction, resulting in the strains NQ1350, NQ1357.

Construction of the *cra* deletion strain (NQ1077): The *Δ cra* deletion allele in strain LJ2801 (*E. coli* Genetic Stock Center, Yale Univ.), in which a Km^r gene is substituted for the *cra* gene, was transferred to wildtype NCM3722, resulting in the strain NQ1077.

Construction of the PykF, PfkA and ArgA overexpression strains (NQ1543, NQ1544, NQ1545): Overexpression plasmids pNT3 from the library from Saka *et al.*[33] expressing the genes *pykF*, *pfkA* and *argA* respectively from P*tac*, were purified and transformed into wildtype NCM3722, resulting in the strains NQ1543, NQ1544 and NQ1545.

Construction of glpK22 strain (NQ898): To create a strain that grows faster on glycerol, the *glpK* gene in NCM3722 was replaced with the *glpK22* variant[17] by two P1 transduction steps. First, the *pfkA*::km marker was transferred into NCM3722 by phage P1vir, prepared from the Keio collection. The resulting strain (NQ632) from the transduction cannot utilize mannitol as sole carbon source. Second, phage P1vir prepared from CGSC5511 (Lin-43)[16] harboring *glpK22* was infected into NQ632. Selecting a colony that grew on mannitol minimum medium yielded a strain, NQ898, that harbors *glpK22* mutation in NCM3722 background.

Construction of YCE44: The recipient strain NCM3722 was used for P1 transduction[34] with P1 lysate prepared from the Keio collection to create the fliC::Kan mutant. This mutant was then transformed with the Pcp20 plasmid[32] to flip out the Kanamycin marker. The resultant strain was then used as a recipient strain for P1 transduction with BO37[35] (3) P1 lysate to create the final target strain, YCE44 (NCM3722, fliC::FRT-FRT, glmS::PRNAI-mCherry1–11-mKate-T1 terminator-FRT Kan FRT::pstS). The donor strain BO37 was kindly provided by Somenath Bakshi (Paulsson Lab, Harvard Medical School).

Strains used in this study.—Except for BW25113 wildtype used as a control, all the strains used are derived from E. coli K-12 strain NCM3722[36,37] provided kindly by Sydney Kustu lab. See Supplementary Methods for details of strain construction. See Table S1 for summary of strains.

Growth of bacterial culture

Growth media: Unless otherwise indicated, we used N$^+$C$^+$ minimal medium[38], which contains K_2SO_4 (1 g), $K_2HPO_4.3H_2O$ (17.7 g), KH_2PO_4 (4.7 g), $MgSO_4.7H_2O$ (0.1 g), and NaCl (2.5 g) in one liter, and is supplemented with 20 mM NH_4Cl and the specified carbon sources. Carbon sources concentrations were based on the number of carbon atoms in the molecule: 20 mM for C_6-carbons, 30 mM for C_4-carbons and 40 mM for C_3-carbons.

The base minimal medium used for the anaerobic growth of *E. coli* NCM3722 consisted of KH_2PO4 (2 g), K_2HPO4 (14.8 g), NaCl (0.58 g), NH_4Cl (0.54g), and Na_2SO_4 (0.07 g), and 1000x mineral solution (1 mL) per liter. One liter of the 1000x mineral solution contained $MgCl_2$ (60 g), $CaCl_2$ (5.5 g), $FeSO_4.7H_2O$ (5.5 g), $MnCl_2$ (19.7 mg), $CoCl_2$ (23.8 mg), Ni_2SO_4 (26.2 mg), $CuCl_2$ (15.9 mg), $(NH_4)_2MoO_4$ (23.5 mg), SeO_2 (11 mg), $ZnSO_4$ (28.7 mg), and H_3BO_4 (6.2 mg) dissolved in 100 mM HCl. For the consistency of comparison, aerobic the same medium was used for the aerobic growth of NCM3722 reported in Extended Data Fig. 9. Carbon sources were added as indicated.

The medium used for the anaerobic growth of *B. thetaiotaomicron* was the same as that used for the anaerobic growth of *E. coli* but also included 2 mg cyanocobalamin, 2 mg hemin, and 0.6 g cysteine per liter. To make the media anoxic, Hungate tubes (16 mm × 125 mm) filled with 7 mL medium were shaken at 270 rpm under a 7% CO_2, 93% N_2 atmosphere pressurized to 1.5 atm for 75 min. Cultures were transferred anoxically into Hungate tubes with disposable syringes.

Growth measurements: Batch culture aerobic growth was performed in a 37°C water bath shaker or air incubator shaking at 250 rpm. The culture volume was at most 10 ml in 25 mm × 150 mm test tubes. For seed culture, one colony from fresh LB agar plates was inoculated into liquid LB and cultured at 37°C with shaking. Cells were then diluted into the minimal medium and cultured in 37°C water bath shaker overnight (pre-culture). The overnight pre-culture was allowed to grow for at least 3 doublings. Cells from the overnight pre-culture was then diluted to OD_{600} = 0.005–0.025 in identical pre-warmed minimal medium, and cultured in 37°C water bath shaker (experimental culture). 200 μl cell culture was collected in a Sterna sub-micro cuvette for OD_{600} measurement using a thermal spectrophotometer every half doubling of growth after allowing at least 4 generations of growth. The time taken for each sample collection is < 30 sec and had no measureable effect on cell growth.

Anaerobic growth was performed similarly with a few exceptions: All growth for *B. thetaiotaomicron* was carried out in Hungate tubes. For seed culture, a single colony from Wilkens-Chalgren agar plates were inoculated into anoxic Hungate tubes filled with 7mL Wilkens-Chalgren broth and incubated at 37°C with shaking. Cells were then diluted ~300 fold into pre-culture medium to grow overnight. The next day, cells were diluted to OD_{600}= 0.01–0.025 for experimental cultures in the same medium as the pre-culture. OD_{600} measurements for cells in Hungate tubes were made with a Thermo Genesys 20 modified to hold Hungate tubes in place of a cuvette. To keep the culture tube temperature stable, tubes were removed from the water bath shakers to measure OD_{600} and returned within 30 seconds. The OD_{600} measured through the Hungate tubes was equivalent to the OD_{600} measured through a cuvette in the range of at least 0.04 – 0.5.

Anaerobic growth of *E. coli* NCM3722 was measured similarly as *B. thetaiotaomicron* except seed cultures were performed aerobically in LB broth before being diluted ~300 fold into anoxic Hungate tubes for overnight pre-culture with the same media as the experimental culture. Cells were again diluted into fresh Hungate tubes with OD_{600} = 0.01–0.025 for experimental culture and growth was measured with the modified Thermo Genesys 20.

pH Changes: Because anaerobic growth of *E. coli* and *B. thetaiotaomicron* involves copious acid production, the pH of cultures were monitored. Typical pH changes for the anaerobic growth of NCM3722 were from 7.2 (fresh anoxic medium) to 6.7 (at OD_{600} ~ 0.4). For *B. thetaiotaomicron*, the pH changes were from 7.2 (fresh anoxic medium) to 6.9 (OD_{600} ~0.4). The pH for the aerobic growth of NCM3722 stayed around 7.4–7.3 for fresh medium and cultures at OD_{600} ~0.4.

Medium shift and determination of lag times

***E. coli* growth:** Exponentially growing cultures in preshift condition were obtained following the protocol outlined above for growth measurements in tubes or flasks for metabolomics and proteomics experiments. Cultures were grown up to OD_{600}~0.5 before the shift was performed. Cells were then carefully transferred to a filter (previously washed with Milli-Q water) to remove preshift medium and washed twice with warmed postshift medium (at least twofold the volume of culture transferred to the filter). The filter was then moved to a sterile 50ml Greiner tube with warmed postshift medium and cells were gently resuspended from the filter by pipetting. Cells were then diluted in warmed postshift medium to OD_{600}~0.05 for the purpose of lag time measurements and to OD_{600}~0.5 for the purpose of metabolomics and proteomics measurements and incubated. The entire shift was typically completed in under 5 minutes. Lag times were determined as follows: After cells reached steady-state growth in postshift condition, about three to four OD_{600} data points were fitted with an exponential function. The intersection of the fitted exponential and initial postshift OD_{600} was used to determine the lag time.

To screen combinations of carbon sources using a plate reader, the protocol was slightly modified. After being transferred to the filter, cells were washed twice and resuspended using warmed medium without a carbon source. Cells were then diluted into the pre-warmed Thermo Fisher Scientific Nuclon 96 well bottom flat transparent plates filled with different postshift media. These plates covered with a lid were then incubated and culture density was monitored using a Tecan Infinite M200 plate reader at 37°C shaking at 880 rpm to measure lag times. Lag times were determined by fitting the growth curve over the range, where maximal exponential growth rate was reached, by the function $OD(t) = OD_{init}\exp[\lambda(t - T_{lag})]$, which is an exponential growth curve with growth rate λ that is shifted by the lag time T_{lag}. OD_{init} is the OD_{600}, measured just after the shift and the fit parameters were the growth rate growth rate λ and the lag time T_{lag}. The fit was performed using the ‘fit’ command of Gnuplot, which is an implementation of the nonlinear least-squares (NLLS) Marquardt-Levenberg algorithm.

***B. subtilis* growth:** A single colony of *B. subtilis* 3610 was inoculated in 3 ml LB in the morning as a seed culture at 37°C. In the evening, the seed culture was diluted into minimal medium containing various carbon sources: 20 mM glucose, 20 mM mannose, 20 mM maltose and 40 mM glycerol to ensure exponential growth the next day. The seed culture was then diluted to an OD_{600} of 0.025. When the culture reached an OD_{600} of 0.2–0.3, the cells were centrifuged, washed with prewarmed postshift medium, and shifted to minimal medium containing 60 mM Acetate. The OD values were recorded by BioTek Synergy H1 microplate reader.

Yeast growth: Overnight seed cultures of *S. cerevisiae* YPS128 and YPS163 were grown in chemically defined synthetic complete media[39–41], containing 2 % (w/v) glucose. The next day, the seed culture was diluted to an OD_{600} of 0.025 in synthetic complete medium containing various single carbon sources: 2 % (w/v) of glucose, galactose, maltose or raffinose and incubated at 30°C. When cultures reached the exponential phase (OD_{600} of 0.2–0.4), cells were washed twice with prewarmed postshift medium and shifted to the postshift medium containing 2% (w/v) acetate. Growth was followed and OD_{600} values were recorded in a BioTek Synergy H1 microplate reader. The chemically defined synthetic complete media used for this yeast carbon switch experiment left out inositol completely to ensure that cells were only growing one a single carbon source.

Mother machine methods: We use a microfluidic platform based on the ‘mother machine’ design[42], to track individual cells during lag phase. We monitor the morphology of individual cells as they experience media switch under controlled conditions and use the morphological measurements to obtain both growth rate and lag times of individual cells (single-cell lag time analysis).

The mother machine microfluidic device, where cells grow and divide in narrow trenches and are fed by diffusion by an orthogonal feeding channel, has been used for long term tracking of cells[42,43] under tightly controlled local conditions. The Paulsson lab has recently developed a microfluidic platform for tracking cell lineages along the growth curve (Bakshi, S., Leoncini, E., Baker, C., Cañas-Duarte, S., Okumus, B. and Paulsson, J., bioRxiv 2020.03.27.006403), where a batch culture is connected to a microfluidic chip. We use this platform to obtain lag time information at single-cell level (see Extended Data Fig. 3a). Cells from YCE44 strain (expressing constitutively mCherry1–11-mKate) were loaded in a mother machine chip and were allowed to recover for several hours in N+C+ glucose minimal medium before starting imaging. A flask with glucose medium inoculated with YCE44 strain was then connected to the microfluidic device, so that the cells in the chip share the same environment as the cells in the flask. The platform enables us to monitor the OD of the batch culture at high frequency (30 seconds), and to grow the culture under usual laboratory conditions (37°C on orbital shaker, 220rpm). This allows us to monitor the behavior of the batch culture and individual cells synchronously. To perform the shift to acetate, cells in the flask were washed twice with postshift acetate minimal medium and resuspended in postshift acetate minimal medium as described in the batch protocol above. After the shift, cells kept growing for some time at the same growth rate both in the flask and in the microfluidic chip, possibly because some glucose medium was still present in the system. After about 60 minutes, glucose ran out and the cells underwent a diauxic shift. We kept monitoring cells in the Mother machine over the course of the lag phase, as they responded to changes in the batch culture. The experimental protocol is illustrated in Extended Data Fig. 3b.

Conditions of cells in the microfluidic chip are not identical to the ones in the flask since, for instance, cells under observation are diffusely fed in the growth trenches. We minimized this effect by using shorter growth trenches (20μm in length). Also, in order to reduce mixing of glucose and acetate media at the time of switch, we introduced a waste line before the microfluidic chip, which allows to divert the flow at the time of switching, to better control the switch dynamics for the cells in the mother machine.

Imaging Parameters: Images were acquired using a Nikon Ti inverted microscope equipped with a temperature-controlled incubator (OKO lab), an Andor Zyla 4.2 camera, a 40x Phase 2 Plan Apo (numerical aperture NA 0.95, Nikon), an automated motorized stage (Nikon) and Lumencor SpectraX light source. All images were acquired with a 1.5x post-magnification, and the camera-objective combination gave a 0.11 μm/pixel. Focal drift was controlled by the Nikon Perfect Focus System. The timelapse imaging and automatic stage movements were controlled by Nikon NIS Elements software. We imaged cells in phase contrast and RFP channel. Images were taken every 15 minutes with 200ms exposure in order to reduce photobleaching and phototoxicity.

Image analysis pipeline:

Segmentation (FIJI).—After trying few segmentation approaches both using FIJI and Python, we opted for using FIJI macro in combination with manual selection of trenches. Individual lineages were first selected prior to segmentation, and we discarded trenches with double-loading (where cells loaded side-by-side in a growth trench and grow under stressful conditions and poor feeding) or which were out of focus. Of a total of 1494 starting trenches, 363 did present double loading, 44 trenches got unloaded, 7 mother cells did not wake up after the switch to acetate and 2 cells lysed after the switch, 114 cells were discarded for various reasons (out of focus, poor growth before the shift the acetate). The remaining 964 cells were segmented using the fluorescence channel (RFP) with a custom FIJI algorithm based on thresholding, morphological transformations and adjustable watershed, designed to work for cells with changing sizes (cells significantly change their morphology between glucose and acetate media and along the growth curve). We then proceeded to inspect each mask produced, in order to discard trenches with too many visible segmentation errors which might affect the single-cell lag time analysis. Of the 964 trenches segmented, we selected 685 with near-perfect segmentation.

Analysis (Matlab).—We focused solely on the cells at the top of the growth trenches (‘mother cell’), since we can follow these cells for the entire experiment, and we can extract single-cell traces for the full duration. The temporal information of the cell data (such as length and area) was then compiled into single-cell length traces. We identified cell divisions by using a *findpeaks* package by looking at sudden decreases in cell length but still filtering out fluctuations from segmentation mistakes.

From a total of 685 mother cells with near-perfect segmentation, we removed 3 cells that had missing measurements along the time trace or got unloaded from the microfluidic trench. We checked also for cells with no divisions during experiment or after the switch, for filamenting cells (>8μm in length) and cells not recovering after the switch. One cell exhibited filamentation and we proceeded with analysis of the remaining 681 cells.

We estimated that the media should flow through the microfluidic chip at around frame 47 (11.75h from starting of imaging). In order to confirm this determination of the time of the switch to acetate medium in the Mother machine microfluidic chip, we used the single-cell instantaneous growth rate. We observed that cells started to slow down growth at frame 47 (11.75h) and they globally reached a minimum at frame 50 (12.50h). In the rest of the analysis, we used frame 47 as the switching time to acetate medium and frame 50 as starting time for the lag time computation.

In order to compute the lag time for each individual cell, we needed to compute the growth rate at single-cell level. We used the instantaneous growth rates of individual cells determined from changes in cell length between adjacent timepoints for each birth-to-division event (see Extended Data Fig. 3c). The lag time for each individual cell could then be computed using the following formula:

$$T_i^{lag}(t) = t - \frac{1}{\lambda_i^{ACE}} \int_0^t \lambda_i(t) dt,$$

where $\lambda_i(t)$ is the instantaneous growth rate of cell i at time t, λ_i^{ACE} is the maximum growth rate that cell i attains in acetate medium. We used the time of minimum growth rate for the population (frame 50) as starting point for the computation of the lag time (time 0 in previous formula). The lag time from the equation above is a monotonically increasing function of time, and it reaches a plateau when the growth rate approaches λ_i^{ACE}. This plateau corresponds to the single-cell lag time and the resulting distribution is shown in Extended Data Fig. 3d (one of the cells was removed from the analysis since it did not wake up in acetate medium and the analysis was performed on a total of 680 cells).

Using the mother machine, we follow the initial population of cells loaded into the device. However, variability in growth of individual lineages must be considered when comparing results from mother machine data at population level with the batch culture, since cells in the mother machine are not subjected to the dilution effect as it happens in batch. Assuming that the progeny of each cell in the mother machine maintain the same growth characteristics as that progenitor cell, and assuming the same initial cell size, we can calculate the expected batch dynamics from the single cell data in the mother machine. If we denote with $\lambda_i(t)$ the growth rate of cell i in the mother machine at time t and $\lambda_b(t)$ is the instantaneous growth rate of the batch population, then the normalized batch OD_{600} is given by

$$OD_b(t)/OD_b(0) = exp\left(\int_0^t \lambda_b(s)\, ds\right) = \frac{1}{N_0} \sum_{i=1}^{N_0} exp\left(\int_0^t \lambda_i(s)\, ds\right),$$

where N_0 is the number of cells that we observe in the mother machine and time 0 is the time when population attained a minimum in growth rate (frame 50). This equation can be used to calculate the batch growth rate $\lambda_b(t)$ from single-cell data and to derive the expected lag time for the batch culture $T_b^{lag}(t)$:

$$T_b^{lag}(t) = t - \frac{1}{\lambda_b^{ACE}} log\left[\frac{1}{N_0} \sum_{i=1}^{N_0} exp\left(\int_0^t \lambda_i(s)\, ds\right)\right],$$

where λ_b^{ACE} is the maximum of the expected batch growth rate $\lambda_b(t)$ in acetate medium and the integral is performed to the timepoint where $\lambda_b(t) = \lambda_b^{ACE}$. When the growth rate reaches its steady-state, $T_b^{lag}(t)$ is invariant for different integration times t.

Because the experimental setup includes high-frequency OD_{600} measurements (30 seconds interval) of the connected batch culture flask (see Extended Data Fig. 3e), we could use these data to compute the batch lag time and have a direct comparison between the batch culture and the single-cell data. Similarly to the previous formula, the lag time for the batch culture can be computed using the formula:

$$T^{lag}(t) = t - \frac{1}{\lambda_{ACE}} log\left(\frac{OD(t)}{OD(0)}\right)$$

where λ_{ACE} corresponds to the maximum growth rate in acetate medium and we consider as t=0 the time at which the bulk culture halts growth after switch to acetate. The lag time of the batch corresponds to the value of $T^{lag}(t)$ when the growth rate in the flask approaches λ_{ACE}, which corresponds to a plateau for the function $T^{lag}(t)$.

Batch microscopy

Experimental protocol: NCM3722 wildtype cells were grown in N+C+ glucose medium as described above. When the batch culture reached 0.2 OD_{600}, cells were harvested by filtering and washed twice in N+C+ acetate medium (same as for all other medium shift experiments described above). After the washing step, cells were resuspended in N+C+ acetate medium to reach a final OD_{600} of 0.05. This culture was split in two identical 6 well glass bottom plate (cellvis, No 1.5), 5 ml culture in each well. One of the 6 well plate was centrifuged at 4800Xg for 3 min and bacterial cells were imaged on a Nikon Ti2 microscope (40X air phase contrast objective). The plate was kept stationary on the microscope in a 37°C incubator. Phase contrast images were taken from multiple fields of views with a frame rate of 300 second. The other 6 well plate was taken to a shaker air incubator (kept at 37°C, with 220 rpm). This plate was considered as the batch culture control. We measured OD_{600} from this plate and the batch lag time (295 min) was calculated from the recorded optical density measurements (see Extended Data Fig. 4).

Analysis of the microscopy data: After recording the microscopy data, we performed the image analysis using a custom analysis pipeline in Python. Briefly, each time series was first corrected for XY drift using the rigid body stack registration algorithm[44]. After drift correction, single cell time traces were segmented using Otsu thresholding. We stopped tracing a cell when the cell divided, or the field of view got obstructed by adjacent dividing cells, or the cell got dislodged from the glass surface. Cells that we managed to follow for 43 or higher number of frames are considered for analysis. This threshold was chosen based on a systematic analysis of different values for this threshold. We want to establish an upper bound on the number of non-growing cells after the shift to acetate. We do not expect non-growing cells to be overrepresented in transiently present cells that briefly settle on the glass bottom and then swim away. These transiently present cells become more important for low values of this threshold. On the other hand, for high values of this threshold we are artificially enriching for non-growing cells. The intermediate value for the threshold that we chose establishes the most stringent upper bound for the fraction of non-growing cells in the population. We segmented 1761 cells, after which we set an arbitrary threshold of 10% increase in single cell area to identify cells that showed significant growth. In Extended Data Fig. 4, cell traces that crossed the chosen threshold of 10% increase in area are marked in blue and the single cell time traces that showed less than 10% increase in area are marked in red. Out of 1761 segmented single cell traces, 1500 cell traces crossed the chosen growth threshold of 10% increase in area and only 261 single cell traces showed less than 10% increase in area over the time frames that we managed to follow them. Our method sets an upper bound on the cell population, which did not grow more than 10% (in terms of area) within the time frame that we managed to follow them. Most likely, many of these cells would have showed significant growth at later time points, which we were unable to measure due to experimental limitations. This suggests that the actual population of cells that do not resume growth is in reality much smaller than the roughly 14.8% that we have measured. Our observation shows that most cells (1500 out of 1761, more than ~85.17%) show significant growth and only a small fraction (261 out of 1761, ~14.83%) grew less than 10% over the observable timeframe (see Extended Data Fig. 4).

Metabolite mass spectrometry

Sample collection and quenching: For metabolite measurements and ^{13}C labeling experiments, an amount proportional to 1 mL*OD_{600} of the culture broth was transferred onto a 0.45 μm pore size Durapore filter (Millipore) and vacuum-filtered. For metabolite measurements, the filter with cells was immediately transferred after filtration into 4 mL of 20°C acetonitrile/methanol/water (2:2:1) to quench metabolism and 200 μL of a uniformly ^{13}C labeled *E. coli* metabolite extract were added as internal standard[45]. ^{13}C labeling experiments were performed immediately after vacuum-filtration on the filter, as described previously[46]. Specifically, cells on the filter were first washed with fresh, preheated (37°C) acetate M9 medium for 10 sec and ^{13}C labeling was initiated by changing the washing solution to preheated (37°C) M9 medium containing uniformly ^{13}C labeled acetate. After each labeling step, the filter was transferred into 4 mL of 20°C acetonitrile/methanol/water (2:2:1) for quenching. To extract metabolic intermediates, the filter was kept in this solution at -20°C for 1 h. Then, the cell debris was removed from the extracts by centrifugation (4°C, 10,000 rpm, 10 min), the supernatants transferred into new tubes and dried to complete dryness.

Sample preparation: For LC/MS analysis, dried extracts were resuspended in 100 μL deionized water of which 10 μL were injected into a Waters Acquity UPLC (Waters Corporation, Milford, MA) with a Waters Acquity T3 column coupled to a Thermo TSQ Quantum Ultra triple quadrupole instrument (Thermo Fisher Scientific) with negative-mode electrospray ionization. Compound separation was achieved by a gradient of two mobile phases (A) 10 mM tributylamine, 15 mM acetic acid, and 5% (v/v) methanol and (B) 2-propanol[47]. Acquisition of mass isotopomer distributions of carbon backbones was done as previously described[48]. Peak integration was performed by an in-house software (Begemann and Zamboni, unpublished).

Kinetic flux estimation: Flux estimation closely followed Yuan *et al.*[49], based on the kinetics of incorporation of a ^{13}C acetate isotope. At multiple time points, after cells were rapidly switched from unlabeled to isotope-labeled acetate, LC/MS analysis was performed. Resulting plots of unlabeled compound versus time were fitted by an exponential decay and the flux was calculated as the decay rate multiplied by the intracellular metabolite concentration.

Proteomic mass spectrometry

Metabolic labeling with ^{15}N[50] provides relative quantitation of unlabeled proteins with respect to labeled proteins across growth conditions of interest. Each experimental sample in a series is mixed in equal amount with a known labeled standard sample as reference, and the relative change of protein expression in the experimental sample is obtained for each protein.

Sample collection: For each culture, 1.8 ml of cell culture at OD_{600}=0.4~0.5 was collected by centrifugation. The cell pellet was re-suspended in 0.2 ml water and fast frozen on dry ice.

Sample preparation: A balanced mixture of the two 15N labeled cell samples (glycolytic and gluconeogenic growth conditions by growing cells on glucose and acetate respectively) was prepared as a universal reference. 100 μg of the labeled reference proteome was added to 100 μg of each experimental sample. This balanced preparation (equal amounts of total protein) enables the measurement of proteome mass fraction for each protein. Furthermore, the mixed reference is used to ensure the distribution of proteins in the reference is not strongly biased by a particular growth condition.

Proteins were precipitated by adding 100% (w/v) trichloroacetic acid (TCA) to 25% final concentration. Samples were left to stand on ice for a minimum of 1 hour. The protein precipitates were spun down by centrifugation at 13,200 g for 15 min at $4^{o}C$. The supernatant was removed, the pellets were washed with cold acetone, and dried in a Speed-Vac concentrator.

The pellets were dissolved in 80 μl 100 mM NH_4HCO_3 with 5% acetonitrile (ACN). 8 μl of 50 mM dithiothreitol (DTT) was added to reduce the disulfide bonds before the samples were incubated at $65^{o}C$ for 10 min. Cysteine residues were modified by the addition of 8 μl of 100 mM iodoacetamide (IAA) followed by incubation at $30^{o}C$ for 30 min in the dark. The proteolytic digestion was carried out by the addition of 8 μl of 0.1 μg/μl trypsin (Sigma-Aldrich, St. Louis, MO) with incubation overnight at $37^{o}C$. The peptide solutions were cleaned by using the PepClean® C-18 spin columns (Pierce, Rockford, IL). After drying in a Speed-Vac concentrator, the peptides were dissolved into 10 μL sample buffer (5% ACN and 0.1% formic acid).

Mass spectrometry: The peptide samples were analyzed on an AB SCIEX TripleTOF® 5600 system (AB SCIEX, Framingham, MA) coupled to an Eksigent NanoLC Ultra® system (Eksigent, Dublin, CA). The samples (2 μL) were injected using an autosampler. The samples were first loaded onto a Nano cHiPLC Trap column 200μm × 0.5mm ChromXP

C18-CL 3μm 120Å (Eksigent) at a flow rate of 2 μL/min for 10 minutes. The peptides were then separated on a Nano cHiPLC column 75μm × 15cm ChromXP C18-CL 3μm 120Å (Eksigent) using a 120-min linear gradient of 5–35% ACN in 0.1% formic acid at a flow rate of 300 nL/min. MS1 settings: mass range of m/z 400–1250 and accumulation time 0.5 seconds. MS2 settings: mass range of m/z 100–1800, accumulation time 0.05 seconds, high sensitivity mode, charge state 2 to 5, selecting anything over 100 cps, maximal number of candidate/cycle 50, and excluding former targets for 12 sec after each occurrence.

Protein identification: The raw mass spectrometry data files generated by the AB SCIEX TripleTOF® 5600 system were converted to centroided mzml files, which were searched using the X!Tandem search engine (thegpm.org) against the *E. coli* proteome database (Uniprot) to identify proteins. The following parameters were used in the X!Tandem searches: parent mass error 50 ppm, fragment mass error 100 ppm. Ions with charge 1, 5, 6, or 7 were ignored, as were peptides of less than six residues. Spectral libraries for each each condition were built and refined using Spectrast (ISB), only keeping peptides that were identified in three or more individual samples, and collapsing individual spectra into a consensus spectra for each peptide.

Relative protein quantitation: The raw mass spectrometry data files were converted to the .mzML format using conversion tools provided by AB Sciex, and the consensus libraries from Spectrast were used to quantify each of the (non-centroided) .mzML files using our in-house quantification software[8] (Massacre). Briefly, the intensity for each peptide is integrated over a patch in RT, m/z space that encloses the envelope for the light and heavy peaks. After collapsing data in the RT dimension, the light and heavy peaks are fit to a multinomial distribution (a function of the chemical formula of each peptide) using a least squares Fourier transform convolution routine[9], which yields the relative intensity of the light and heavy species. The ratio of the non-labeled to labeled peak intensity is obtained for each peptide in each sample. A confidence measure for each fit is calculated from a Support Vector Machine trained on a large set of user scoring events.

The relative protein level for each protein in each sample is obtained as a ratio by taking the weighted median (using the SVM score) of the ratios of all its corresponding peptides.

Uncertainty of individual measurements

Biological replicates show the following typical uncertainties in measured quantities: growth rate, ~5%; lag times,~15% for long lag times (>1h). Short lag times (<1h) show higher relative variabilities.

Extended Data

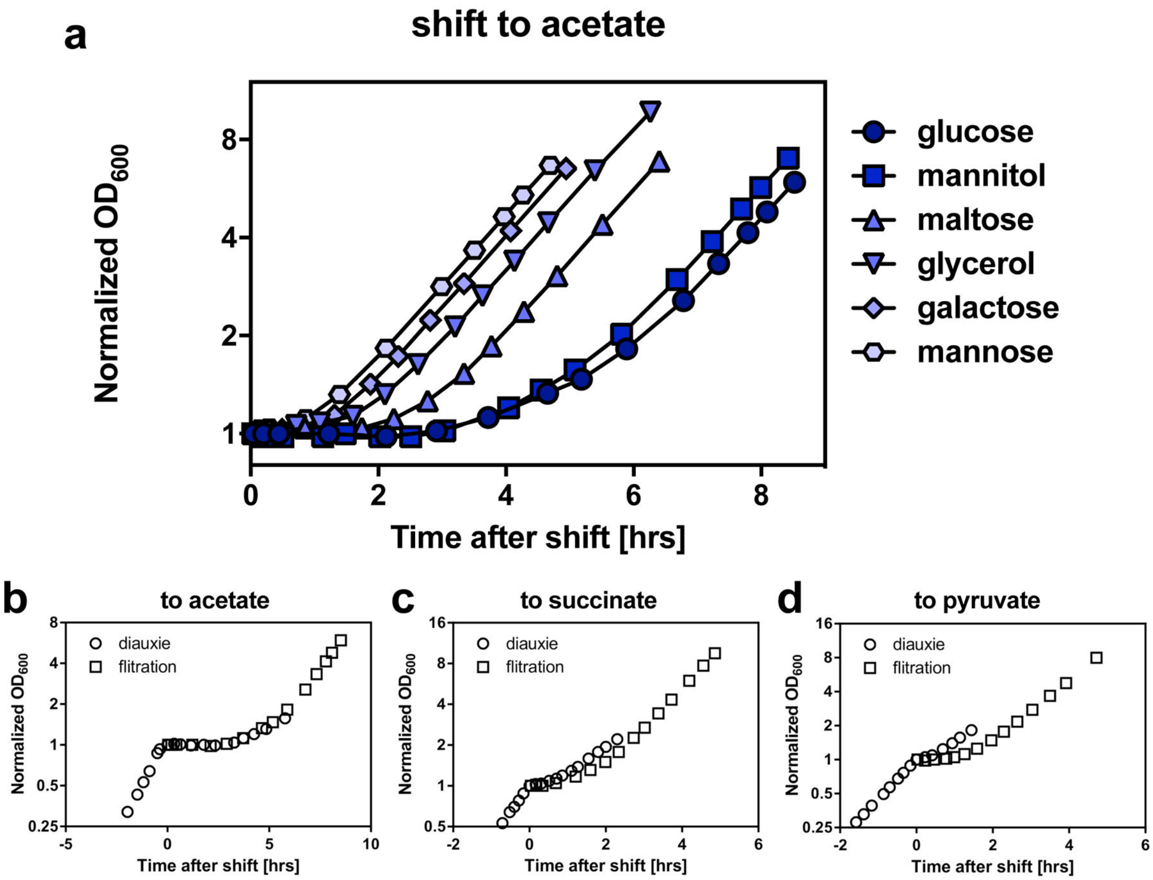

Extended Data Fig. 1: Growth curves for shifts.

a, Shifts from different glycolytic carbons to acetate by filtration. Long lag phases can consist of several hours without detectable biomass production. There are large variations in the duration of lag phase in the shift to acetate between different preshift carbon sources. The duration of lag phase correlates with preshift growth rate. Fast growth before the shift results in very long lag times. **b-d,** Comparisons of lag times from filtration shifts and diauxie. **b,** 1.7mM glucose to 60mM acetate. **c,** 1.7 mM glucose to 30 mM succinate. **d,** 1.7 mM glucose to 40 mM pyruvate. Lag times resulting from filtration shifts and from classical diauxie experiments are mostly comparable. In the case of pyruvate (panel c), the presence of pyruvate in the medium in addition to glucose adversely affected the growth rate resulting in a shorter lag time in the diauxie shift, consistent with our general observation of the growth rate dependence of lag times.

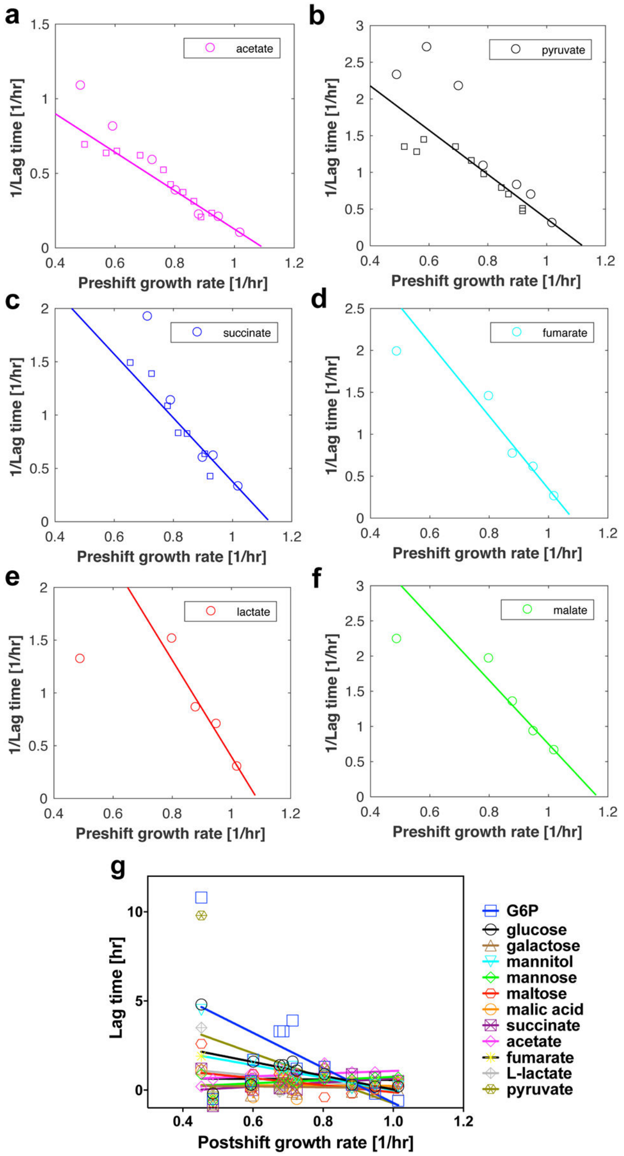

Extended Data Fig. 2: Lag time growth rate relations.

a-f, Inverse of resulting lag times as a function of preshift growth rate in glycolytic conditions. Each panel summarizes shifts to a particular postshift medium: **a,** to acetate; **b,** to pyruvate; **c,** to succinate; **d**, to fumarate; **e,** to lactate; **f**, to malate. Preshift growth rate was modulated via different carbon sources (circles) and via lactose uptake titration (squares). Solid lines are non-linear least-squares fits (MATLAB lsqcurvefit function) of lag times as a function of preshift growth rates by the relation given by Eq. [1]. Most lag phases agree very well with Eq. [1] and only some shifts with short lag times (low growth rates) deviate somewhat from the relation given by Eq. [1]. This is partly the result of plotting inverse lag times, which amplifies relatively small experimental variations of lag times for short lag phases. These fits allow us to estimate 95% confidence intervals for model parameters (MATLAB nlparci function), most importantly for the critical growth rates λ_0. Acetate: $\lambda_C = (1.10 \pm 0.01)$/hr, $\alpha = 0.78 \pm 0.10$, $n = 17$; pyruvate: $\lambda_C = (1.12 \pm 0.03)$/hr, α

$=0.33\pm0.07$, $n=17$; succinate: $\lambda_C = (1.13\pm0.04)$/hr, $\alpha=0.33\pm0.09$, $n=14$; fumarate: $\lambda_C = (1.08\pm0.02)$/hr, $\alpha=0.23\pm0.07$, $n=5$; lactate: $\lambda_C = (1.09\pm0.05)$/hr, $\alpha=0.22\pm0.15$, $n=5$; malate: $\lambda_C = (1.17\pm0.09)$/hr, $\alpha=0.22\pm0.11$, $n=5$. **g,** Lag times as a function of steady-state growth rates in the postshift medium for different preshift media. Colored solid lines are linear regressions of the corresponding colored data points. Carbon source that allow a slower growth rates tend to result in longer lag phases, when they are the postshift carbon sources. This intuitive correlation has previously been characterized[13].

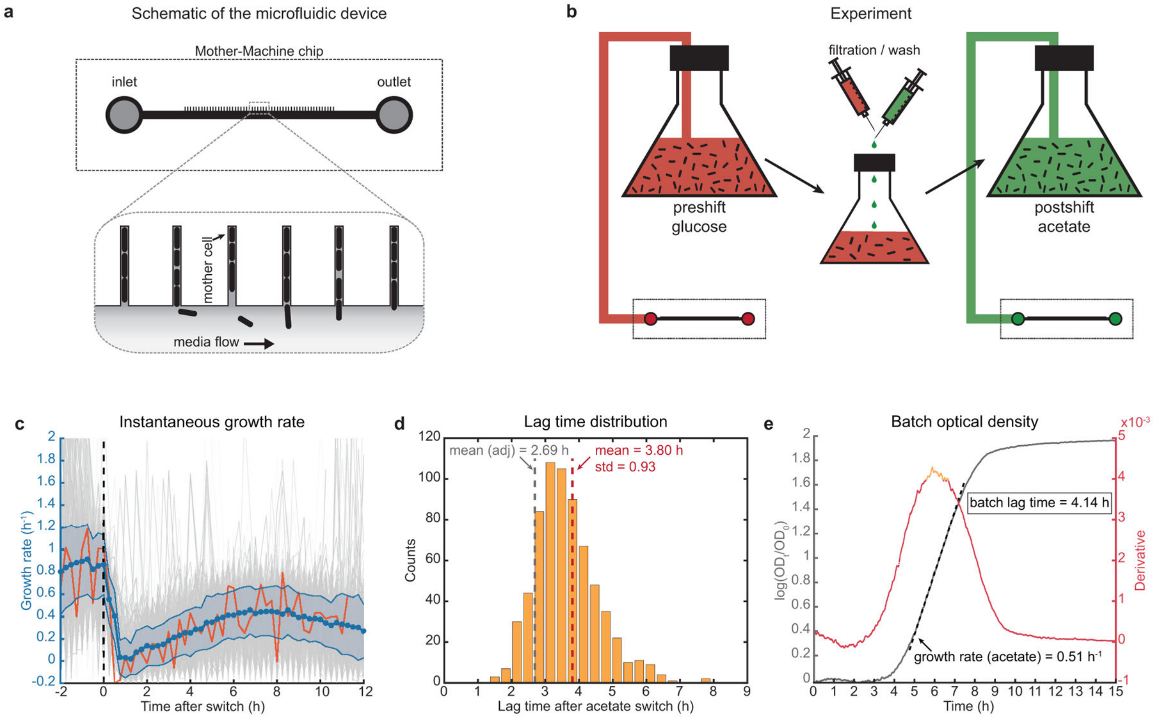

Extended Data Fig. 3: Single cell behavior during glucose to acetate shift in microfluidics.

a. Schematic of the microfluidic device (mother-machine) in which bacterial cells are grown. The cells are loaded in narrow trenches (inset), where they are diffusively fed from the media flowing through the feeding lane. As cells grow out of the trenches, they are washed away by the media flow. We focused solely on the cells at the bottom of each trench, also called 'mother cells', since they are kept for the entire duration of the experiment. **b.** Experiment schematic. Cells were recovered in the mother machine using glucose medium, and then connected to a flask with culture growing in the same medium[28]. Media switch was performed the same way as for the batch cultures, and the flow was then restarted towards the mother machine. We noticed that cells continued growing for a short time after filtration both in batch and in the Mother machine, presumably because of residual glucose in the system and therefore the experiment most resembles a diauxic shift. **c.** Instantaneous single-cell growth rates determined from cell length. Individual cells length traces were used to compute instantaneous growth rates. The light blue points and shaded area around them represent the population average and standard deviation of the single-cell instantaneous growth rates. The orange trace is the instantaneous growth rate trace of an exemplary cell. **d.** Single-cell lag time distribution. Lag time is defined as the time delay in growth after the switch as compared to instantaneous growth at the maximum postshift growth rate. The instantaneous growth rate traces were used to compute single-cell lag times (see Materials and Methods section for details). The red dashed line is the mean of the lag time distribution of the tracked cells. Cells tracked in the Mother machine introduce a bias for long lag times, because growing cells are washed away instead of being amplified as happens in the batch culture. Therefore, we also calculated the expected batch lag time (2.69 h), when taking into account growth of cells as described in the Materials and Methods section (gray dashed line). **e.** Growth curve of the batch culture connected to the microfluidic after the shift was used to determine lag time of the connected batch culture (4.14 h). The quantitative agreement between the microfluidics and the batch is not perfect. Nevertheless, the single-cell distribution of lag times establishes that the response of individual cells after the shift is unimodal and that the lag time is not governed by a small sub-population of cells that grows immediately on acetate as expected by Kotte et al.[12]. We see no reason why this population of cells should not be present in the microfluidics if it were present in the batch. Our data also showed no evidence for the prediction by Kotte et al.[12] that most cells would never recover and grow after the shift. However, because the cells were grown in a microfluidic chip, this experiment cannot definitively rule out that the recovery of growth observed here is due to differences in the conditions. To determine if such a non-growing population exists in the batch culture, we performed another experiment as described in Extended Data Fig. 4.

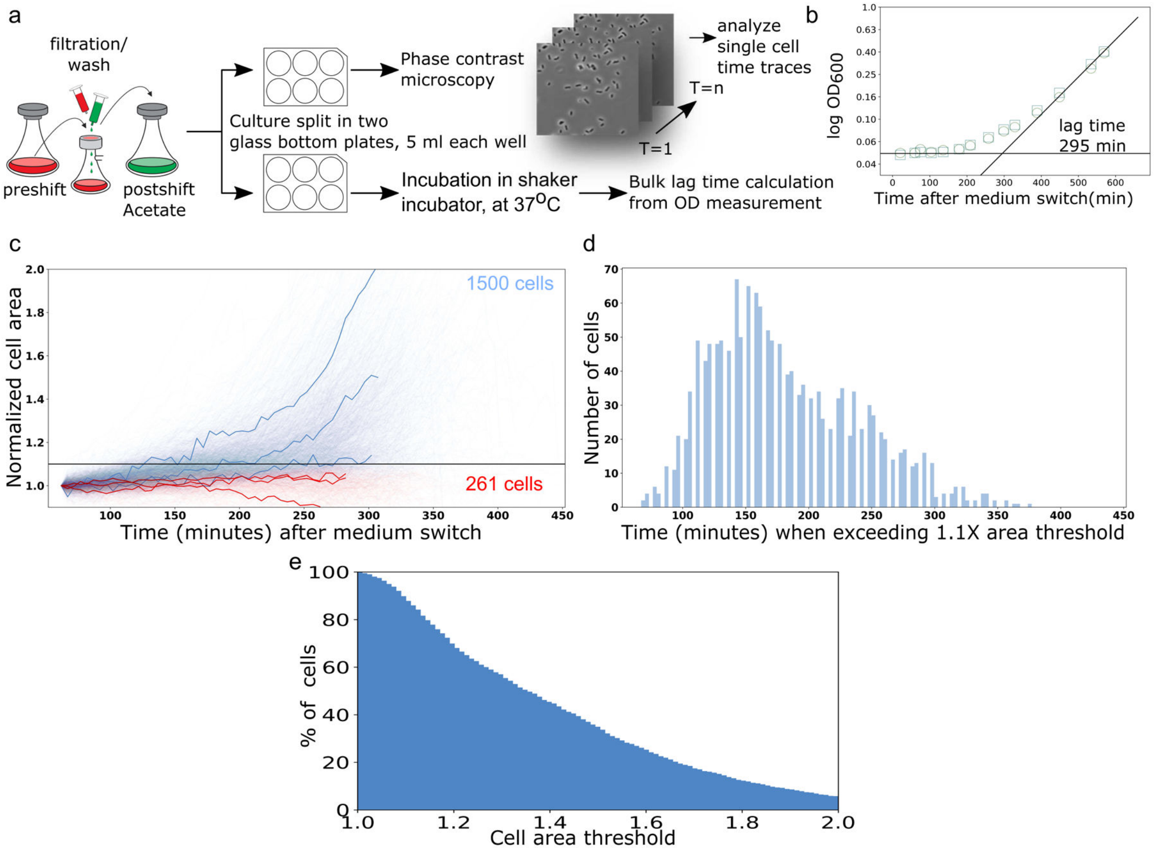

Extended Data Fig. 4: Single cell behavior during glucose to acetate shift via time-lapse microscopy of batch culture:

a, Schematic illustration of the experimental protocol (see Supplementary Materials and Methods, Batch microscopy). After the medium shift from glucose to acetate, the culture was split into two identical 6-well glass bottom plates. One was briefly centrifuged and placed into an incubator on a microscope for time-lapse microscopy. The other was placed in a shaker incubator as a control, and OD_{600} was monitored manually. **b,** Growth curves from two biological repeats (circles and squarters), obtained by monitoring OD_{600} from the control 6-well plate after the media switch. The calculated lag time is 295 min, virtually identical to the batch culture lag time that we characterized in the shift from glucose to acetate (Fig. 1), indicating that the environment of the 6-well plate is almost identical to that of the batch culture as far as the lag time is concerned. **c,** Normalized single-cell-area traces from two biological repeats taken with the microscope in the other plate (n=1761, total number of trace). We use cell area as a metric for biomass growth. Light blue traces indicate cells that crossed an arbitrary 10% area-increase threshold within the time of our observation (see Materials and Methods, Batch microscopy). Red traces indicate the cells that did not cross the 10% threshold. We observed 1500 cells crossing the threshold, while 261 did not cross it -- before they became unobservable, either because they detached from the glass or were flooded by other cells. **d,** Histogram showing the distribution of the time it takes for individual cells to increase its area by 10%. **e,** Plot showing the fractions of cells (y axis) that grew in cell area by at least the amount shown on the x axis, relative to their initial size. These data show that the vast majority of cells recovers after an initial lag phase, eventually growing on acetate. Despite the relatively short observation window of 5–6 hours, roughly equal to the batch lag time (when cells are flooded by other faster growing cells and cannot be further observed by microscopy), the data establish that the vast majority of cells exhibits substantial growth (see panel e). For example a 10% increase in cell area is easily detectable and we observed that 85% of cells crossed this threshold. We note that cells that crossed this threshold grew continuously over the course of observation and exhibited a single-cell growth curve and lag time (seen panels c & d), similar to the batch lag time. This indicates that no more than 15% of cells were completely growth arrested after the shift to actetate, even during this very limited window of observation. This shows that in the lag phases that we study here, the dormant subpopulations proposed previously[12] played a negligible role for determining lag times. (As an example, even if we assume the ~15% non-growing cells observed never ever recover growing again, they would only contribute ~21 minutes to the total lag time of 295 minutes).

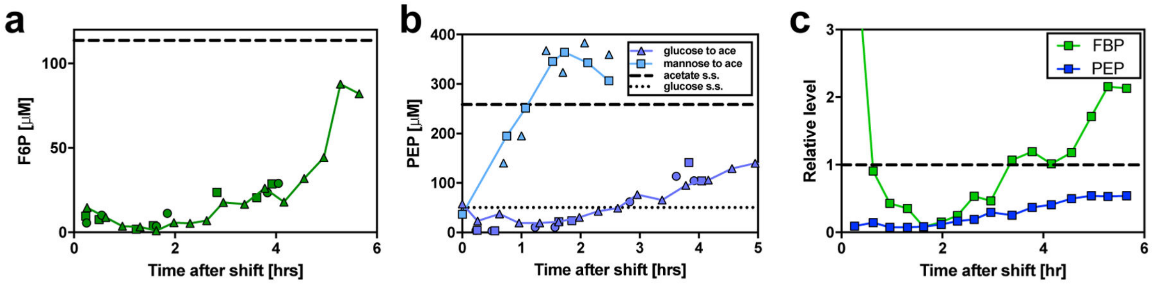

Extended Data Fig. 5: Absolute and relative concentrations of key metabolites in a shift from glucose to acetate.

a, Intracellular concentration of F6P the 3 biological repeats of the shift from glucose to acetate presented in Fig. 2 of the main text. The dashed line represents the steady state level of F6P for growth on acetate. The concentration of F6P is low compared to Michaelis constants of key enzymes Pgi and TktA, which catalyze the first reactions from F6P for the production of essential precursors for biomass production E4P and R5P. **b,** Intracellular concentration of PEP over the course of lag phase for a shift from glucose to acetate (red symbols) and a shift from mannose to acetate (green symbols). Steady-state concentrations on glucose and acetate are indicated by the dashed lines. PEP is a key repressor of glycolytic flux by inhibiting Pfk[29]. The concentration of PEP remained low throughout lag phase, even compared to the steady-state concentration on glucose (dotted line), where Pfk is very active. **c,** Time courses of FBP and PEP concentrations throughout lag phase in a shift from glucose to acetate. Concentrations of FBP and PEP were normalized by their steady-state concentration during exponential growth on acetate. FBP drops from its steady-state level for growth on glucose, which is more than 100-fold higher than the steady-state level on acetate (normalized to 1). PEP remains at very low concentrations and slowly builds up together with FBP 1.5 h after the shift. In the framework of our model, we attribute this phase to the slow increase in gluconeogenic enzymes from protein synthesis.

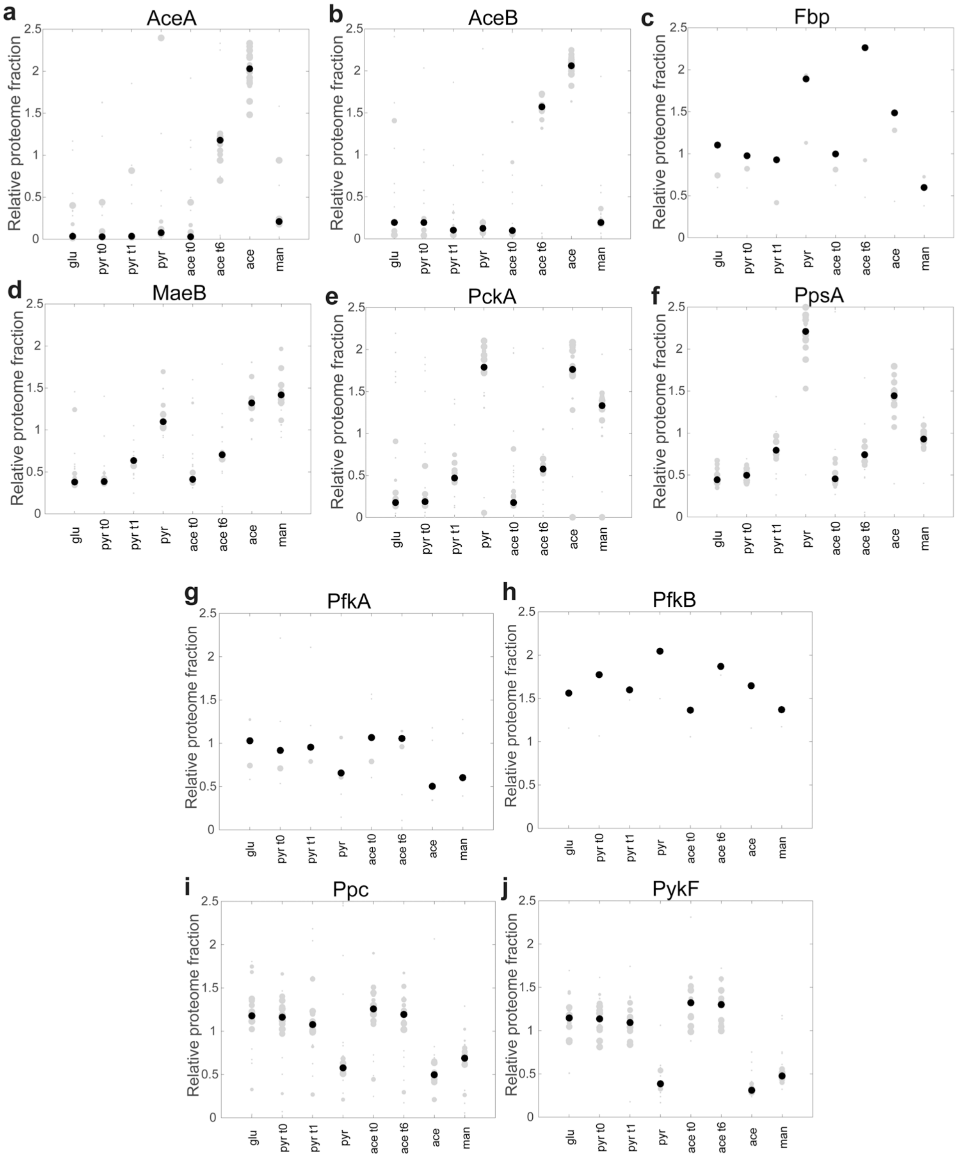

Extended Data Fig. 6: Proteomics characterization of lag phase dynamics.

a-f, Gluconeogenic enzymes. Relative levels of gluconeogenic enzymes at different times during lag phase from glucose to acetate (ace t0: immediately after the shift, ace t6: exiting lag phase, 6 hours after the shift) and glucose to pyruvate (pyr t0: immediately after the shift, pyr t1: exiting lag phase, 1 hour after the shift) and in different steady state conditions glucose (glu), pyruvate (pyr), acetate (ace). **a,** isocitrate lyase (AceA); **b,** malate synthase (AceB); **c,** fructose-1,6-bisphosphatase (Fbp); **d,** malate dehydrogenase (MaeB); **e,** phosphoenolpyruvate carboxykinase (Pck); **f,** PEP synthase (Pps). **g-j,** Glycolytic enzymes. Relative levels of irreversible glycolytic enzymes at different times during lag phase from glucose to acetate (ace t0: immediately after the shift, ace t6: exiting lag phase, 6 hours after the shift) and glucose to pyruvate (pyr t0: immediately after the shift, pyr t1: exiting lag phase, 1 hour after the shift) and in different steady state conditions glucose (glu), pyruvate (pyr), acetate (ace). **g,** 6-phosphofructokinase I (PfkA); **h,** 6-phosphofructokinase II (PfkB);

i, PEP carboxylase (Ppc); **j,** pyruvate kinase I (PykF). The black dots indicate the weighted median value, derived from multiple measurements, calculated by using as weights the confidence of a sample's quality, as derived by a support vector model, which was set up to classify samples into "high quality" or "low quality", using a training set of several thousand samples that were classified by hand[15]. The weights' range is [0,1] and can be found as a separate attribute (named *svmPred*) for each sample in the accompanying source file. The grey dots indicate individual measurements and the size of the dot indicates the confidence for this particular measurement (the larger the dot the higher the confidence that this measurement is of high quality). The size of the dot was defined using the "MarkerSize" attribute of the "plot" function in Matlab. In particular, the dot size was calculated as the confidence value of the measurement (*svmPred* attribute in the accompanying file) times 11 (this number was used to allow clearer plotting of the dots and enhancement of the visual inspection capabilities). If the product of this multiplication for a certain measurement was below a certain minimum value (in our case, 1.8), the size of the dot was set to be this minimum, as below that value the dot was not visible with the naked eye.

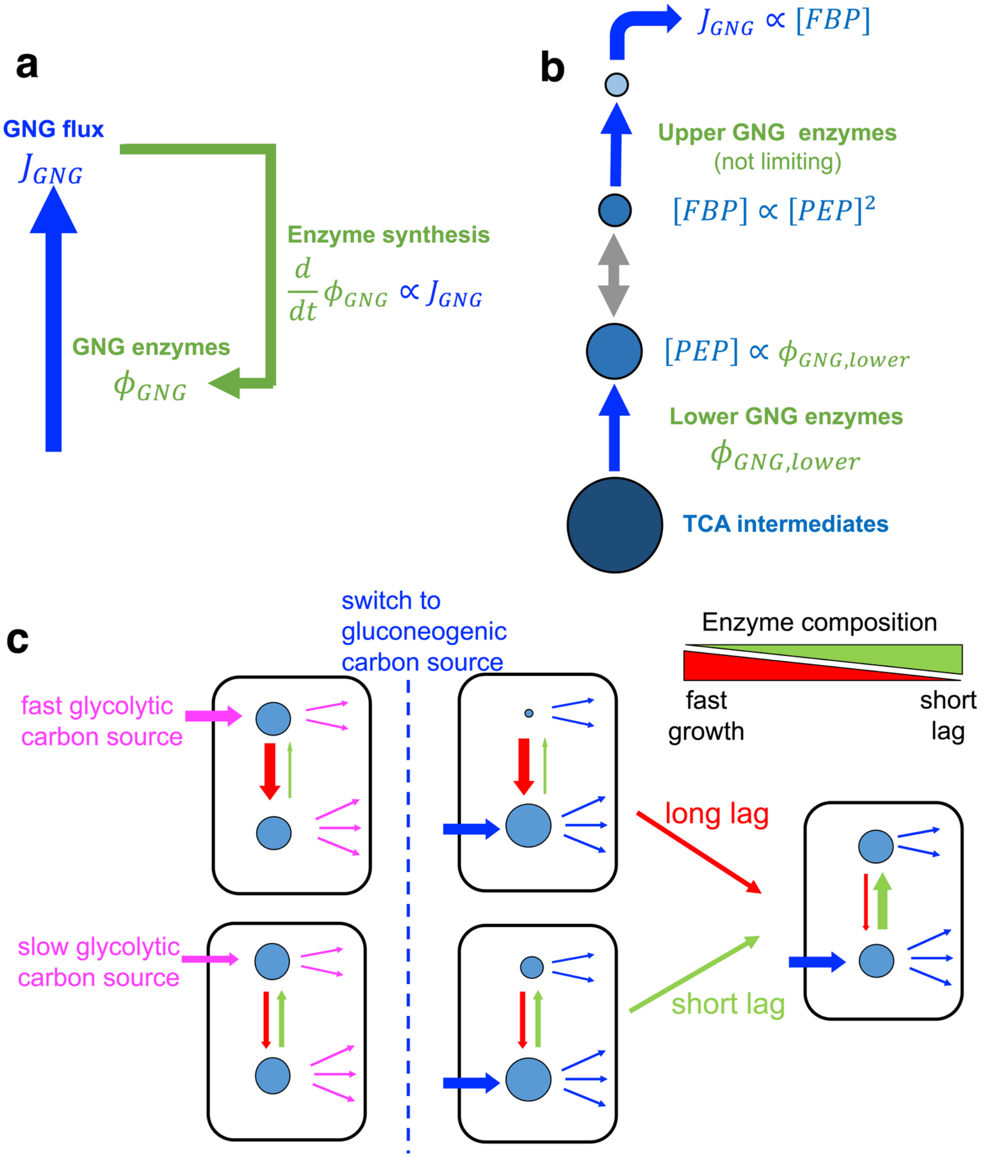

Extended Data Fig. 7: Illustration of sequential flux limitation model and tradeoff between growth and lag.

a, Intuitively, in our model, lag phases emerge because the gluconeogenic flux J_{GNG} (blue arrow) limits protein synthesis (green arrow), which includes the synthesis of gluconeogenic enzymes. Therefore, the production rate of limiting gluconeogenesis is proportional to the gluconeogenic flux

$$\frac{d}{dt}\phi_{GNG,\,lower} \propto J_{GNG}\,. \qquad [a]$$

The gluconeogenic flux J_{GNG}, in turn, depends on limiting metabolite concentrations. **b,** To understand the dynamic scaling of these metabolite concentrations, based on the biochemistry of the pathway, we describe gluconeogenesis by a coarse-grained model comprising two irreversible steps (upper and lower gluconeogenesis), connected by reversible reactions. Upper gluconeogenesis does not appear to be limited by its enzyme (Fbp), whose abundance changed only moderately throughout the lag phase and across growth conditions (see Extended Data Fig. 6 & proteomics data from Hui et al[3]). We thus assume the flux through upper gluconeogenesis (top blue arrows) to be limited by the concentration of its substrate, FBP, i,e, $J_{GNG} \propto [FBP]$. The latter is connected to the output of lower gluconeogenesis, PEP, by the realtion $[FBP] \propto [PEP]^2$ due to the stoichiometry of the reversible reactions (grey arrows). The enzymes of lower gluconeogenesis do appear to be limiting based on previously measured proteomics data[3] (Fig. 3a, Extended Data Fig. 6). We assume that lag phase is dominated by a quasi-stationary phase, where transcriptional regulation can be considered constant and therefore the abundances of gluconeogenic enzymes change throughout the lag phase in proportion to each other, characterized by $\phi_{GNG,\ lower}$. We assume that the abundances of gluconeogenic enzymes change in proportion to each other throughout the lag phase, characterized by $\phi_{GNG,\ lower}$. This assumption is quite plausible as the expression of gluconeogenic enzymes is primarily controlled by a common transcription factor Cra. In support of this assumption, we note that for different preshift (steady-state) conditions, the abundances of different gluconeogenic enzymes are also proportional to each other as they show the same linear growth-rate dependence (Fig. 3a). The flux through lower gluconeogenesis (bottom blue arrow), which is proportional to [PEP], then is governed by $\phi_{GNG,\ lower}$. Thus,$[PEP] \propto \phi_{GNG,\ lower}$, resulting in

$$J_{GNG} \propto \phi_{GNG,\,lower}^2 . \qquad \text{[b]}$$

c, At fast glycolytic growth (top), glycolytic enzymes are highly abundant (thick red arrows), whereas gluconeogenic enzymes are low (thin green arrows). Enzyme composition therefore strongly favors glycolysis, which result in severe depletion of metabolites in gluconeogenesis after the shift to gluconeogenic conditions and a long lag phase. On the other hand, for slow glycolytic growth (bottom), the ratio of glycolytic and gluconeogenic enzymes is much more balanced (red and green arrows of similar thickness), resulting in an improved carbon supply to gluconeogenesis after shift and hence a shorter lag.

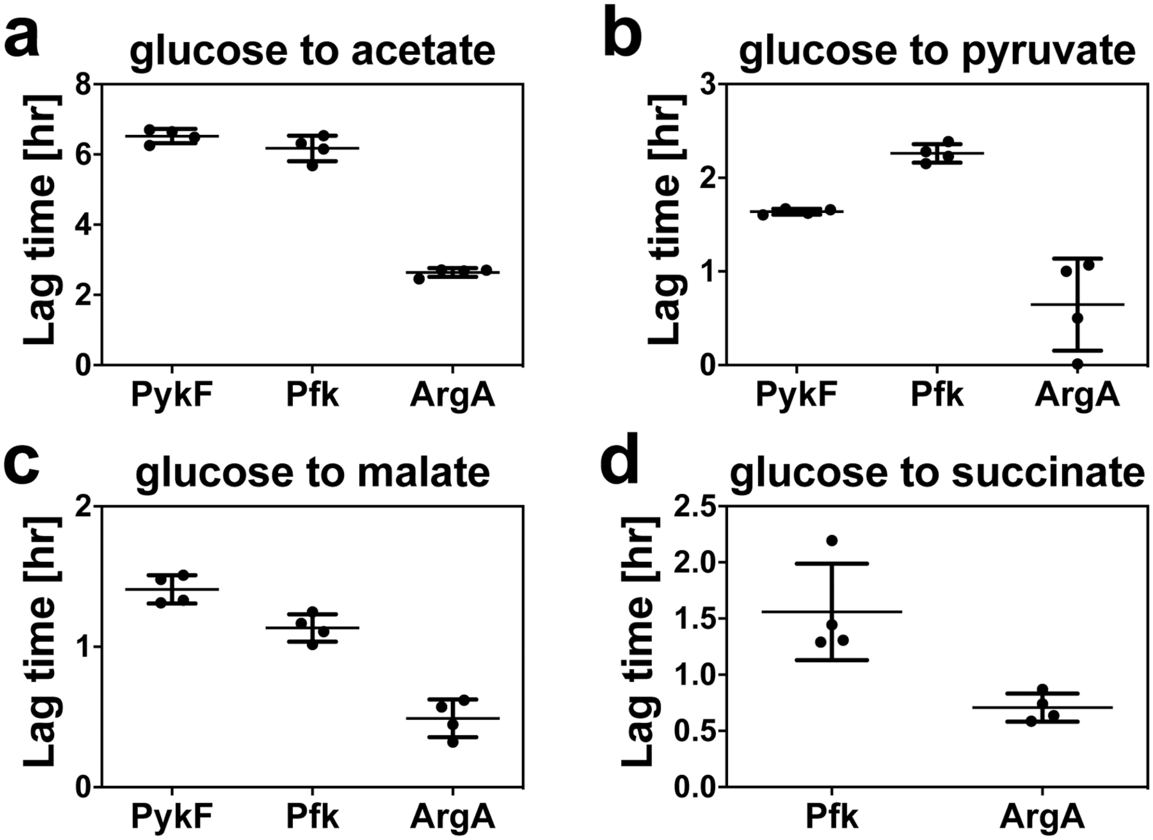

Extended Data Fig. 8: Preshift overexpression of glycolytic enzymes.

Lag times from glucose to **a,** acetate, **b,** pyruvate, **c,** malate, **d,** succinate, with preshift overexpression of glycolytic enzymes PykF (strain NQ1543) or Pfk (strain NQ1544), compared to the preshift overexpression of a control enzyme ArgA (strain NQ1545), with the overexpressed protein all harbored on the same plasmid (pNT3) from the *tac* promoter. Lines and error bars indicate mean and standard deviation (n=4). Lag times more than doubled from preshift overexpression of Pfk or PykF. These results indicate that residual activity of glycolytic enzymes plays an important role in lag phase despite the existence of allosteric regulation of these glycolytic enzymes. Consistent with this picture, the concentration of PEP, a key regulatory metabolite and repressor of glycolytic flux, remained low throughout lag phase, even compared to steady-state levels on glycolytic carbons (see Extended Data Fig. 5).

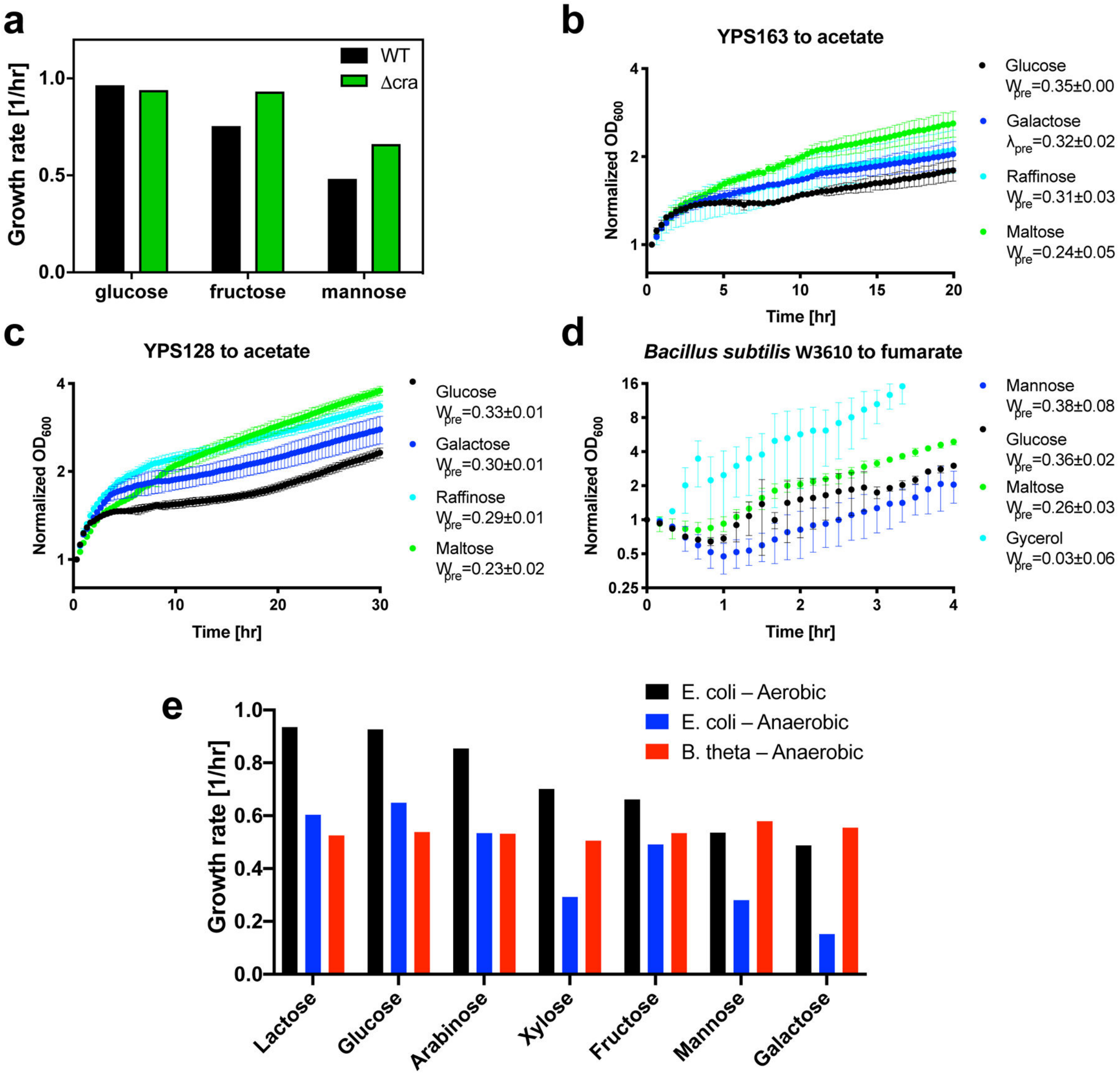

Extended Data Fig. 9: Improved growth of Cra knockout and tradeoff for other microbes.

a, Growth rates of Cra knockout on glycoltic carbon sources. Growth rates on several slow glycolytic carbon sources are significantly improved in the Cra knockout as compared to WT. The Cra knockout expresses very low levels of most gluconeogenic enzymes and glycolytic enzymes are derepressed. As a consequence, a Cra knockout strain cannot grow on most gluconeogenic carbon sources. **b-d,** Growth-adaptation tradeoff in wildtype yeast strains and *B. subtilis*. We grew two different wildtype yeast strains (YPS163 and YPS128), as well as a *B. subtilis* strain at different preshift growth rates, before shifting them to acetate (panel b, c) and fumarate (panel d) minimal medium respectively. After the shift, culture density OD_{600} was monitored as a function of time. Data points indicate the mean and error bars are the standard deviation from 3 biological replicates (n=3). The lag time of the growth curves increases with increasing preshift growth rate (given in the legend), suggesting a tradeoff similar to that characterized for *E. coli* (main text, Fig. 1). **e,** Growth comparison between *E. coli* and *B. thetaiotaomicron*, an obligatory anaerobe. The growth rate of *E. coli* NCM3722 on a number of common carbon substrates from the 'top' (i.e., glycolysis and pentosephosphate pathways) exhibit a range of values from 0.9/h down to 0.5/h (blue bars). The growth rates of *B. thetaiotaomicron* on the same substrates in anaerobic condition (red bars) are all within 10% of each other. For comparison, we also show the growth rates of NCM3722 on the same substrates in anaerobic condition (green bars). They are largely correlated with their aerobic growth rates, with the fast ones comparable to that of *B. thetaiotaomicron* (~0.6/h) and the slow ones at about 1/5 of the fast ones. Saturating amounts of substrates were used, 15mM in all cases except for *E. coli* on mannose where 40mM was used.

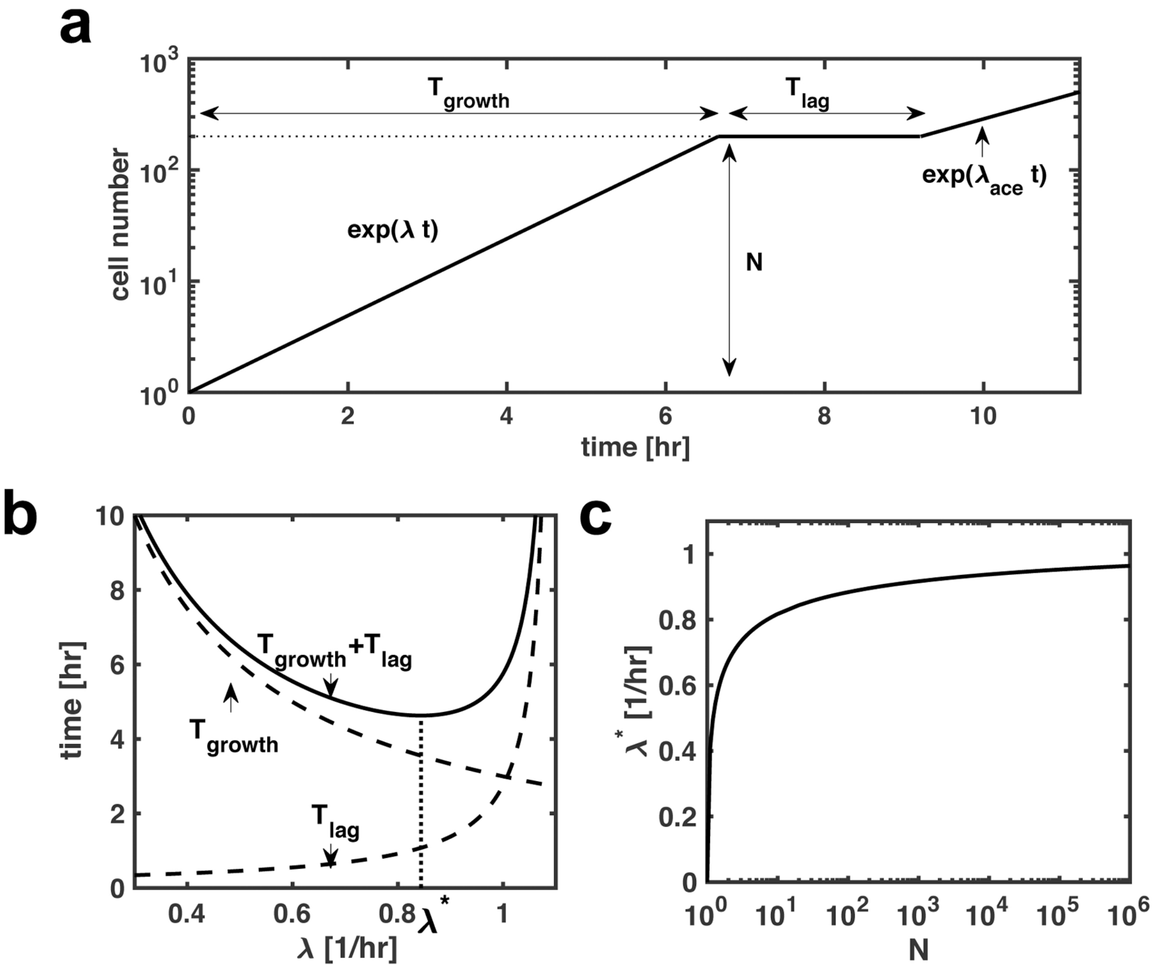

Extended Data Fig. 10: Optimal growth rate as a function of expected abundance of the substrate in the environment.

a, Cell initially grow by a factor N (reflecting the expected carbon abundance) for time T_{growth} at the growth rate λ. When carbon runs out the cells enter lag phase, chartecterized by the lag time T_{lag}. After the lag time, cells again grow exponentially, e.g. on a fermentation product, acetate, at growth rate λ_{ace}. **b,** The optimal strategy for the cell minimizes the total time before postshift exponential growth (resulting in the same cell number, but starting growth first). The total time before postshift growth resumes is the sum of the growth time T_{growth} =log(N)/λ and the lag time, given by Eq. [1] of the main text, T_{lag}=1/[$\alpha(\lambda_0-\lambda)$], both of which are influenced by the growth rate λ. The optimal growth rate λ* minimizes this total time and the expression for λ* is given by

$$\lambda^* = \lambda_0 \frac{\sqrt{\alpha \ln(N)}}{1 + \sqrt{\alpha \ln(N)}}.$$

c, For the strain NCM3722, the expression for the optimal growth rate λ* given Eq. [6] of the main text is plotted versus the expected carbon abundance, given by N. The value of α was determined from the fit in Fig. 1d, to the majority of glycolytic carbon sources (black line). Interestingly, for realistic carbon abundances, the range of optimal growth rates spans precisely the relatively narrow range of growth rates on naturally occurring carbon sources, observed for the wild-type *E. coli* strain NCM3722[2], e.g. glucose (0.95/hr), mannitol (0.90/hr), maltose (0.79/hr), glycerol (0.70/hr), galactose (0.59/hr), mannose (0.49/hr). The optimal growth rate only substantially drops below 0.5/hr, when the expected preshift carbon abundance allows for less than a single doubling $N < 2$, and only surpasses 1.0/hr at enormous, unrealistically high carbon abundances $N > 10^{12}$, explaining the absence of naturally occurring carbon sources that result in such growth rates.

Supplementary Material

Refer to Web version on PubMed Central for supplementary material.

Acknowledgements

We thank Dr. Andrew Murray for helpful comments and suggestions, and Dr. Vadim Patsalo for technical support and development of the proteomics method. Markus Basan acknowledges the SystemsX.ch postdoctoral fellowship. Dr. Tomoya Honda acknowledges the JASSO long-term graduate fellowship award. Work in the Hwa lab is supported by the NIH through grant R01GM109069 and by Simons Foundation (Grant 330378). James R. Williamson acknowledges NIH support through Grant R01GM118850.

Main References

1. Scott M, Gunderson CW, Mateescu EM, Zhang Z & Hwa T Interdependence of cell growth and gene expression: origins and consequences. Science 330, 1099–102 (2010). [PubMed: 21097934]
2. Basan M et al. Overflow metabolism in Escherichia coli results from efficient proteome allocation. Nature 528, 99–104 (2015). [PubMed: 26632588]
3. Hui S et al. Quantitative proteomic analysis reveals a simple strategy of global resource allocation in bacteria. Mol. Syst. Biol (2015).
4. LaCroix RA et al. Use of Adaptive Laboratory Evolution To Discover Key Mutations Enabling Rapid Growth of Escherichia coli K-12 MG1655 on Glucose Minimal Medium. Appl. Environ. Microbiol 81, 17–30 (2015). [PubMed: 25304508]
5. Utrilla J et al. Global Rebalancing of Cellular Resources by Pleiotropic Point Mutations Illustrates a Multi-scale Mechanism of Adaptive Evolution. Cell Syst. 2, 260–271 (2016). [PubMed: 27135538]
6. O’Brien EJ et al. Quantification and Classification of E. coli Proteome Utilization and Unused Protein Costs across Environments. PLOS Comput. Biol 12, e1004998 (2016). [PubMed: 27351952]
7. Towbin BD et al. Optimality and sub-optimality in a bacterial growth law. Nat. Commun 8, 14123 (2017). [PubMed: 28102224]
8. Schuetz R, Zamboni N, Zampieri M, Heinemann M & Sauer U Multidimensional optimality of microbial metabolism. Science 336, 601–4 (2012). [PubMed: 22556256]
9. Shoval O et al. Evolutionary trade-offs, Pareto optimality, and the geometry of phenotype space. Science 336, 1157–60 (2012). [PubMed: 22539553]
10. Tendler A et al. Evolutionary tradeoffs, Pareto optimality and the morphology of ammonite shells. BMC Syst. Biol 9, 12 (2015). [PubMed: 25884468]
11. Reimers A-M, Knoop H, Bockmayr A & Steuer R Cellular trade-offs and optimal resource allocation during cyanobacterial diurnal growth. Proc. Natl. Acad. Sci. U. S. A 114, E6457–E6465 (2017). [PubMed: 28720699]
12. Kotte O, Volkmer B, Radzikowski JL & Heinemann M Phenotypic bistability in Escherichia coli’s central carbon metabolism. Mol. Syst. Biol 10, 736 (2014). [PubMed: 24987115]
13. Baranyi J & Roberts TA A dynamic approach to predicting bacterial growth in food. Int. J. Food Microbiol 23, 277–294 (1994). [PubMed: 7873331]

14. You C et al. Coordination of bacterial proteome with metabolism by cyclic AMP signalling. Nature 500, 301–6 (2013). [PubMed: 23925119]
15. Erickson DW et al. A global resource allocation strategy governs growth transition kinetics of Escherichia coli. Nature 551, 119–123 (2017). [PubMed: 29072300]
16. Zwaig N & Lin ECC Feedback Inhibition of Glycerol Kinase, a Catabolic Enzyme in Escherichia coli. Science 153, 755–757 (1966). [PubMed: 5328677]
17. Pettigrew DW, Liu WZ, Holmes C, Meadow ND & Roseman S A single amino acid change in Escherichia coli glycerol kinase abolishes glucose control of glycerol utilization in vivo. J. Bacteriol 178, 2846–52 (1996). [PubMed: 8631672]
18. Lin ECC Glycerol Dissimilation and its Regulation in Bacteria. Annu. Rev. Microbiol 30, 535–578 (1976). [PubMed: 825019]
19. Freedberg WB, Kistler WS & Lin EC Lethal synthesis of methylglyoxal by Escherichia coli during unregulated glycerol metabolism. J. Bacteriol 108, 137–44 (1971). [PubMed: 4941552]
20. Goelzer A et al. Quantitative prediction of genome-wide resource allocation in bacteria. Metab. Eng 32, 232–243 (2015). [PubMed: 26498510]
21. Maarleveld TR, Wortel MT, Olivier BG, Teusink B & Bruggeman FJ Interplay between Constraints, Objectives, and Optimality for Genome-Scale Stoichiometric Models. PLOS Comput. Biol 11, e1004166 (2015). [PubMed: 25849486]
22. O’Brien EJ, Lerman JA, Chang RL, Hyduke DR & Palsson BO Genome-scale models of metabolism and gene expression extend and refine growth phenotype prediction. Mol. Syst. Biol 9, 693–693 (2014).
23. Yi X & Dean AM Phenotypic plasticity as an adaptation to a functional trade-off. Elife 5, e19307 (2016). [PubMed: 27692064]
24. Fraebel DT et al. Environment determines evolutionary trajectory in a constrained phenotypic space. Elife 6, e24669 (2017). [PubMed: 28346136]
25. Vasi FK & Lenski RE Special section: Stationary-phase mutations in microorganisms Ecological strategies and fitness tradeoffs in Escherichia coli mutants adapted to prolonged starvation. J. Genet 78, 43–49 (1999).
26. Rozen DE, Philippe N, Arjan De Visser J, Lenski RE & Schneider D Death and cannibalism in a seasonal environment facilitate bacterial coexistence. Ecol. Lett 12, 34–44 (2009). [PubMed: 19019196]
27. Ying B-W et al. Evolutionary Consequence of a Trade-Off between Growth and Maintenance along with Ribosomal Damages. PLoS One 10, e0135639 (2015). [PubMed: 26292224]
28. Bakshi S et al. Dynamic Regulation of Growth and Physiology of Microbes under Complex Changing Conditions. bioRxiv 2020.03.27.006403 (2020). doi:10.1101/2020.03.27.006403
29. Fenton AW & Reinhart GD Disentangling the web of allosteric communication in a homotetramer: heterotropic inhibition in phosphofructokinase from Escherichia coli. Biochemistry 48, 12323–8 (2009). [PubMed: 19905012]
30. Brown SD & Jun S Complete Genome Sequence of Escherichia coli NCM3722. Genome Announc. 3, (2015).
31. Klumpp S, Zhang Z & Hwa T Growth rate-dependent global effects on gene expression in bacteria. Cell 139, 1366–75 (2009). [PubMed: 20064380]
32. Datsenko KA & Wanner BL One-step inactivation of chromosomal genes in Escherichia coli K-12 using PCR products. Proc. Natl. Acad. Sci. U. S. A 97, 6640–5 (2000). [PubMed: 10829079]
33. Saka K et al. A complete set of Escherichia coli open reading frames in mobile plasmids facilitating genetic studies. DNA Res. 12, 63–8 (2005). [PubMed: 16106753]
34. Thomason LC, Costantino N & Court DL *E. coli* Genome Manipulation by P1 Transduction. in Current Protocols in Molecular Biology 1.17.1–1.17.8 (John Wiley & Sons, Inc., 2007). doi:10.1002/0471142727.mb0117s79 [PubMed: 18265399]
35. Okumus B et al. Mechanical slowing-down of cytoplasmic diffusion allows in vivo counting of proteins in individual cells. Nat. Commun 7, (2016).

36. Soupene E et al. Physiological studies of Escherichia coli strain MG1655: growth defects and apparent cross-regulation of gene expression. J. Bacteriol 185, 5611–26 (2003). [PubMed: 12949114]
37. Lyons E, Freeling M, Kustu S & Inwood W Using genomic sequencing for classical genetics in E. coli K12. PLoS One 6, e16717 (2011). [PubMed: 21364914]
38. Csonka LN, Ikeda TP, Fletcher SA & Kustu S The accumulation of glutamate is necessary for optimal growth of Salmonella typhimurium in media of high osmolality but not induction of the proU operon. J. Bacteriol 176, 6324–33 (1994). [PubMed: 7929004]
39. Hirsch JP & Henry SA Expression of the Saccharomyces cerevisiae inositol-1-phosphate synthase (INO1) gene is regulated by factors that affect phospholipid synthesis. Mol. Cell. Biol 6, 3320–8 (1986). [PubMed: 3025587]
40. Dowd SR, Bier ME & Patton-Vogt JL Turnover of phosphatidylcholine in Saccharomyces cerevisiae. The role of the CDP-choline pathway. J. Biol. Chem 276, 3756–63 (2001). [PubMed: 11078727]
41. Jesch SA, Zhao X, Wells MT & Henry SA Genome-wide analysis reveals inositol, not choline, as the major effector of Ino2p-Ino4p and unfolded protein response target gene expression in yeast. J. Biol. Chem 280, 9106–9118 (2005). [PubMed: 15611057]
42. Wang P et al. Robust growth of escherichia coli. Curr. Biol 20, 1099–1103 (2010). [PubMed: 20537537]
43. Norman TM, Lord ND, Paulsson J & Losick R Memory and modularity in cell-fate decision making. Nature 503, 481–486 (2013). [PubMed: 24256735]
44. Thévenaz P, Ruttimann UE & Unser M A pyramid approach to subpixel registration based on intensity. IEEE Trans. Image Process 7, 27–41 (1998). [PubMed: 18267377]
45. Wu L et al. Quantitative analysis of the microbial metabolome by isotope dilution mass spectrometry using uniformly 13C-labeled cell extracts as internal standards. Anal. Biochem 336, 164–71 (2005). [PubMed: 15620880]
46. Hörl M, Schnidder J, Sauer U & Zamboni N Non-stationary (13)C-metabolic flux ratio analysis. Biotechnol. Bioeng 110, 3164–76 (2013). [PubMed: 23860906]
47. Buescher JM, Moco S, Sauer U & Zamboni N Ultrahigh performance liquid chromatography-tandem mass spectrometry method for fast and robust quantification of anionic and aromatic metabolites. Anal. Chem 82, 4403–12 (2010). [PubMed: 20433152]
48. Rühl M et al. Collisional fragmentation of central carbon metabolites in LC-MS/MS increases precision of ^{13}C metabolic flux analysis. Biotechnol. Bioeng 109, 763–71 (2012). [PubMed: 22012626]
49. Yuan J, Bennett BD & Rabinowitz JD Kinetic flux profiling for quantitation of cellular metabolic fluxes. Nat. Protoc 3, 1328–40 (2008). [PubMed: 18714301]
50. Oda Y, Huang K, Cross FR, Cowburn D & Chait BT Accurate quantitation of protein expression and site-specific phosphorylation. Proc. Natl. Acad. Sci. U. S. A 96, 6591–6 (1999). [PubMed: 10359756]

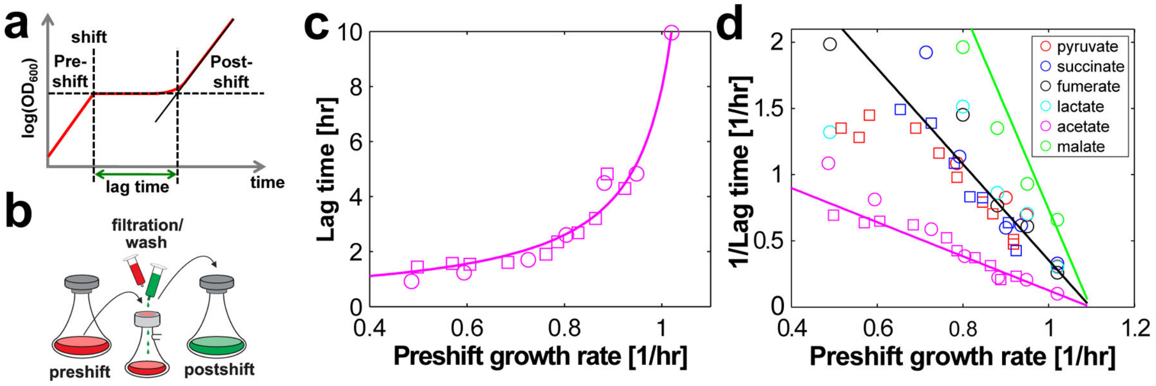

Fig. 1: Phenomenological characterization of lag phase. a,

Schematic illustration of a typical growth curve. Lag time is defined as the time lost in the transition as compared to an instantaneous switch to final steady-state growth. **b,** Illustration of the medium transfer protocol. **c,** Lag times after shifts from different glycolytic carbon sources (circles) and different lactose uptake rates (strain NQ381 with titrable lactose uptake system, squares) to acetate minimal medium. The preshift glycolytic carbon sources from fast growth rates to slow growth rates are glucose 6-P, glucose, mannitol, maltose, glycerol, galactose, mannose, which are all readily metabolized by wildtype *E. coli*, yet result in very different growth rates. The solid line represents the empirical relation given by Eq. [1]. **d,** Inverse lag times for shifts from different glycolytic to gluconeogenic carbon sources, plotted against preshift growth rates. Colors indicates shift to the postshift carbon sources given in the insets; different circles of the same color indicate different preshift carbon sources, while squares indicate the use of titrable lactose uptake in preshift. Lines are non-linear least-mean squares fits of Eq. [1] to data of lag time as a function of preshift growth rate for the shifts to acetate (magenta line), succinate and pyruvate (black line) from our batch culture experiments (Table S2), assuming $\lambda_C \approx 1.1$/hr. For the shift to malate, we performed an additional fit, again assuming $\lambda_C \approx 1.1$/hr (green line). Non-linear least-mean squares fits of Eq. [1] to individual shifts are presented in Extended Data Fig. 2 and the resulting 95%-confidence intervals of paramters are as follows: Acetate: $\lambda_C = (1.10 \pm 0.01)$/hr, $\alpha = 0.78 \pm 0.10$, $n = 17$; pyruvate: $\lambda_C = (1.12 \pm 0.03)$/hr, $\alpha = 0.33 \pm 0.07$, $n = 17$; succinate: $\lambda_C = (1.13 \pm 0.04)$/hr, $\alpha = 0.33 \pm 0.09$, $n = 14$; fumarate: $\lambda_C = (1.08 \pm 0.02)$/hr, $\alpha = 0.23 \pm 0.07$, $n = 5$; lactate: $\lambda_C = (1.09 \pm 0.05)$/hr, $\alpha = 0.22 \pm 0.15$, $n = 5$; malate: $\lambda_C = (1.17 \pm 0.09)$/hr, $\alpha = 0.22 \pm 0.11$, $n = 5$. The mean critical growth rate and standard deviation resulting from the individual fits are given by $\lambda_C = (1.11 \pm 0.03)$/hr.

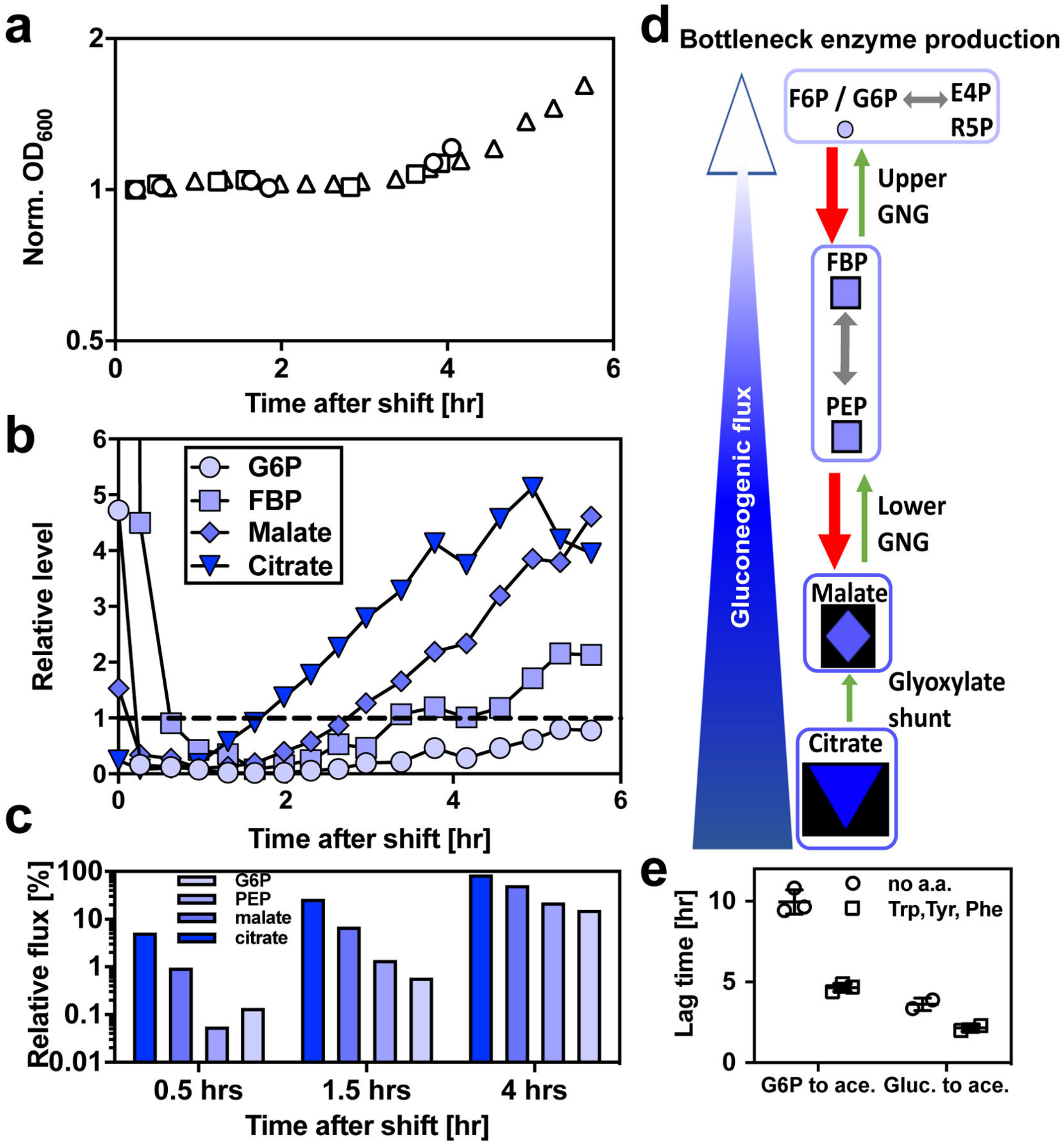

Fig. 2: Metabolic characterization of lag phase during shifts to acetate. a,

Normalized cell density during lag phase of the three shifts from glucose to acetate used for metabolite measurements (triangles) and flux measurements (squares, circles). **b,** Temporal profiles of metabolites, glucose 6-P (G6P), fructose-1–6-bisP (FBP), malate, citrate, throughout lag phase from glucose to acetate normalized by their respective values in postshift medium during exponential steady-state growth (dashed line). Steady-state metabolite concentrations during exponential growth were measured in seperate experiments by taking three metabolite measurements throughout the exponential growth curve for two biological repeats. The metabolite concentrations during the lag phase were then normalized by these steady-state concentrations. Time zero values are measured preshift levels. For FBP this value falls outside the scale (approximately 157). **c,** Fluxes to different metabolites (see panel b) at three time points during the lag phase from glucose to acetate, as a percentage of the steady-state flux during growth on acetate (measured in separate steady-state experiments for two biological repeats). Error bars are standard deviations from biological repeats. **d,** Schematic illustration of glycolysis / gluconeogenesis. The large fading blue arrow indicates the directionality of gluconeogenesis and illustrates the decrease in normalized fluxes and metabolite pools. Green arrows indicate irreversible gluconeogenic reactions catalyzed by gluconeogenic enzymes and red arrows indicate the residual activity of glycolytic enzymes acting in the opposite direction. Erythrose-4-P (E4P) and ribose-5-P (R5P) fructose 6-P (F6P) are derived from fructose 6-P (F6P)/G6P and are required for the biosynthesis of specific amino acids and nucleotides. **e,** The addition of three non-degradable amino acids, Tyrosine (Tyr), Tryptophan (Trp), Phenylalanine (Phe), derived from upper glycolysis to the postshift growth medium substantially reduces lag times in shifts to acetate that we tested from preshift growth on glucose and on glucose 6-P.

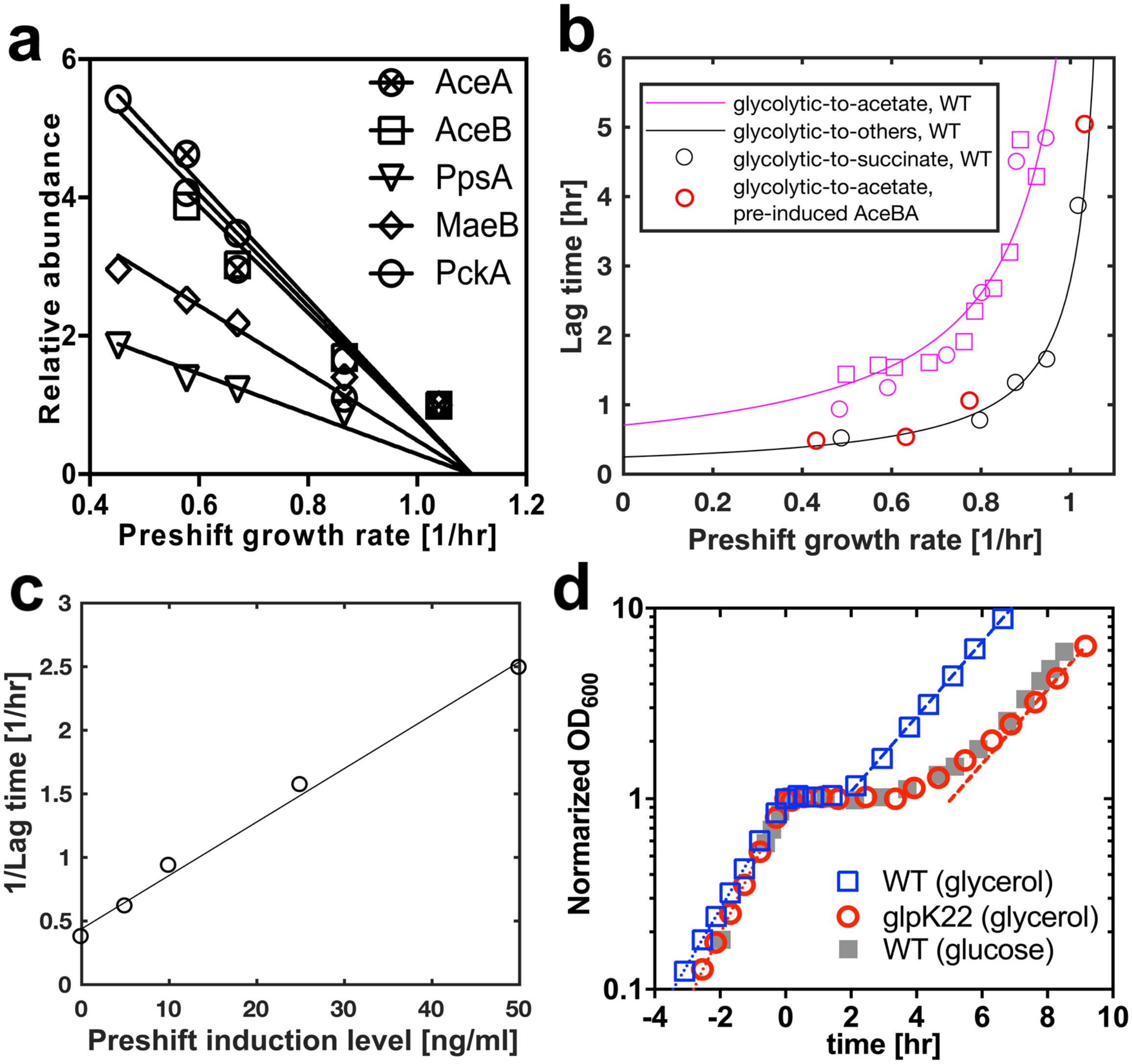

Fig. 3: Tests of model predictions.

a, Relative abundance of gluconeogenic enzymes at different growth rates during steady-state exponential growth in glycolytic conditions; data from Hui *et al.*[3]. Enzymes are isocitrate lyase (AceA), malate synthase A (AceB), phosphoenolpyruvate synthetase (PpsA), malate dehydrogenase (maeB), and phosphoenolpyruvate carboxykinase (PckA). The lines are linear fits assuming a characteristic growth rate λ_C at which lower gluconeogenic enzymes are not expressed anymore, given by $\lambda_C \approx 1.1$/hr, identical to the critical growth rate at which lag times diverge $\lambda_0 \approx 1.1$/hr, determined in Fig. 1c. **b,** Lag times during shifts from various carbon sources to gluconeogenic carbon sources. Magenta lines and symbols represent shifts to acetate for WT cells; data shown in Fig. 1c &1d. Bold red symbols represent reduced lag time for shifts to acetate by a strain with preshift expression of enzymes of the glyoxylate shunt, AceBA. The data fall on the black line, which is the trendline of lag time for shifts by the WT to other gluconeogenic carbon sources shown in Fig. 1d. As an example, the black symbols represent shifts to succinate. **c,** Inverse lag times for shifts from glucose to pyruvate, plotted against different preshift induction levels of phosphoenolpyruvate synthetase (PpsA), for a strain harboring titratable PpsA expression. **d,** Growth of strain NQ898 harboring the glycerol uptake mutant *glpK22* (red)[17] is faster than the wildtype strain NCM3722 in preshift glycerol medium (0.82/hr vs 0.68/hr), but the lag time (as defined in Fig. 1b) upon abrupt shift to acetate at time $t = 0$ is substantially longer (5.1hr vs. 1.9hr). For comparison, the transition of wildtype strain grown in preshift glucose medium (0.87/hr) to acetate is shown in grey. The dashed lines indicate the steady state growth rates of the two strains in acetate, both about 0.45/hr.